Engineered protein-based materials

Obermeyer Research Group

So Yeon Ahn, Rachel Fisher, Aaron Kidane, Jane Liao, Nisha Modi, Brittany Pitt
Department of Chemical Engineering, Columbia University, New York, New York, 10027

Research Group Overview

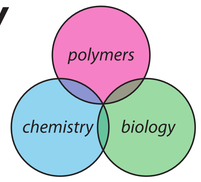

Proteins are an incredible class of polymers. The precise sequence of amino acid monomers is rapidly biosynthesized and encodes the necessary information to transform the simple polymer chain into a folded functional biomacromolecule. Among many amazing properties, protein biopolymers can (1) possess spectacular strength, (2) function as reliable machines and catalysts, and (3) dynamically assemble and disassemble. Our research capitalizes on the diverse structure and function found in native proteins and seeks to engineer complementary functionality into novel protein-based materials. Through genetic modification, we aim to gain responsive control of protein assembly and activity. We strive to create new performance protein based materials for applications in biomedicine and sustainable materials.

Engineered hybrid materials from proteins and polymers

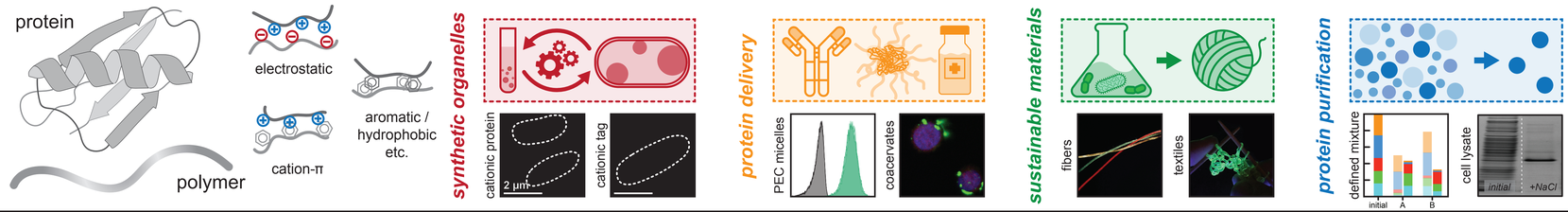

Protein Coacervates

materials properties of engineered protein coacervates

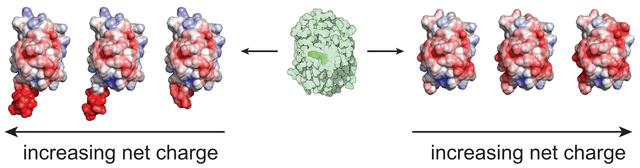

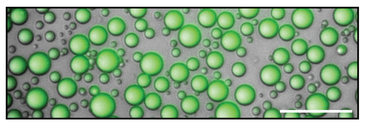

Coacervate droplets formed between supercharged GFP and poly-L-lysine at physiological conditions

Embed particles

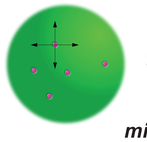

Track tracer particle motion

microscopy

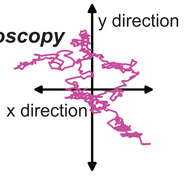

DLS

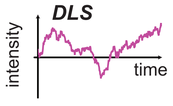

Determine material rheology

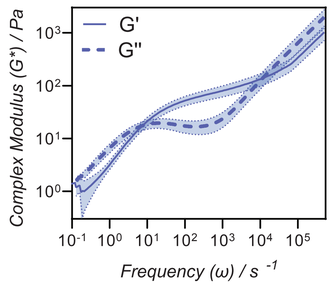

Active Coacervate Materials

feedback via coupled phase separation & enzymatic reaction

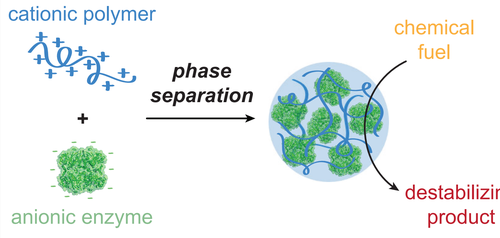

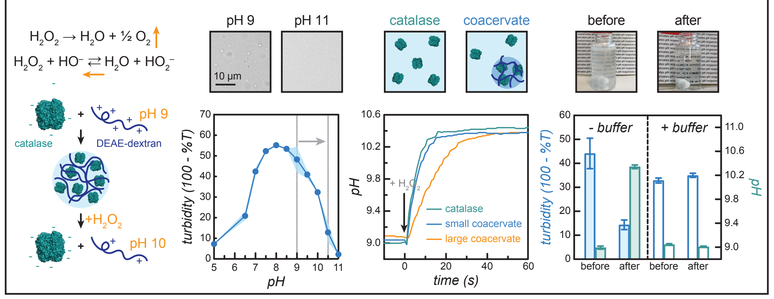

Synthetic Membraneless Organelles

evaluation of single protein phase separation in E. coli

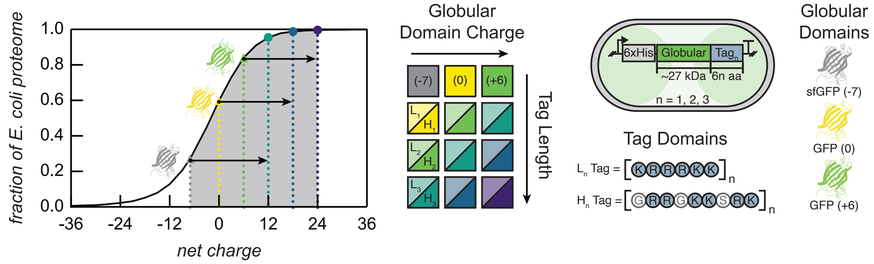

Properties of Synthetic E. coli Condensates

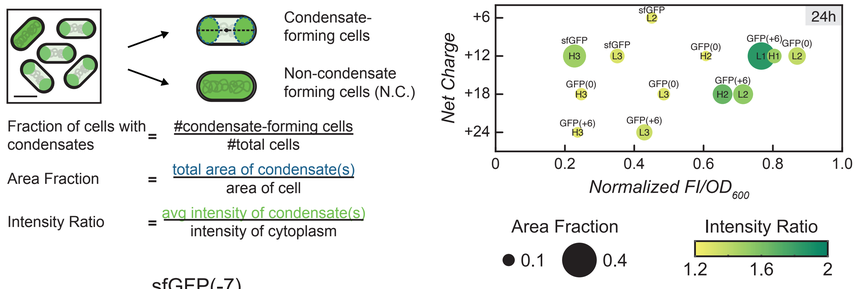

Fraction of cells with condensates = #condensate-forming cells / #total cells

Area Fraction = total area of condensate(s) / area of cell

Intensity Ratio = avg intensity of condensate(s) / intensity of cytoplasm

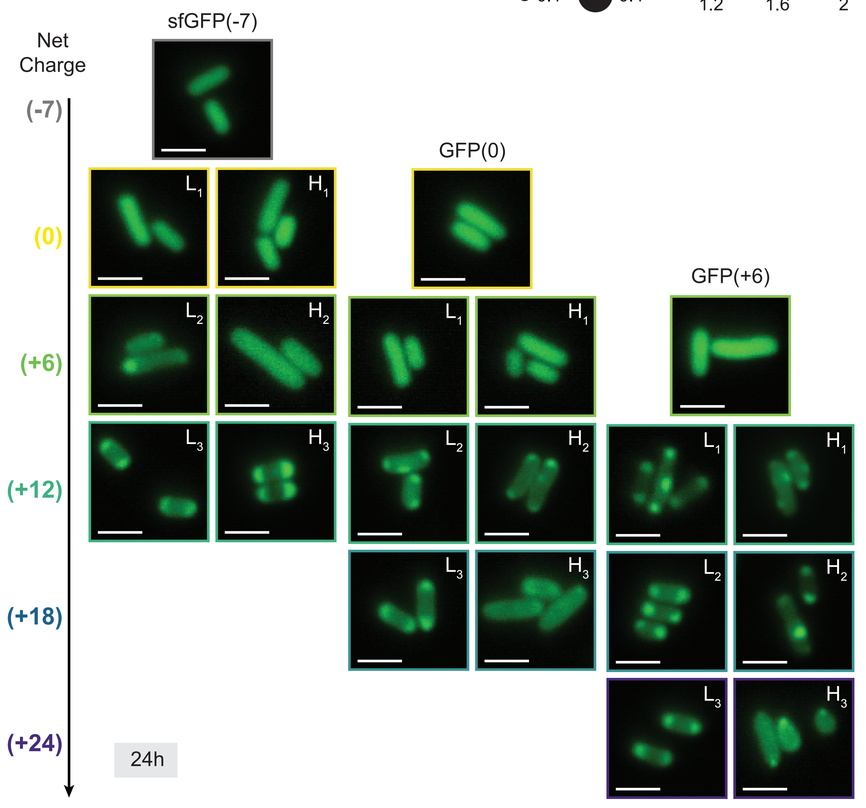

Protein Purification

selectivity of complex coacervation in protein mixtures

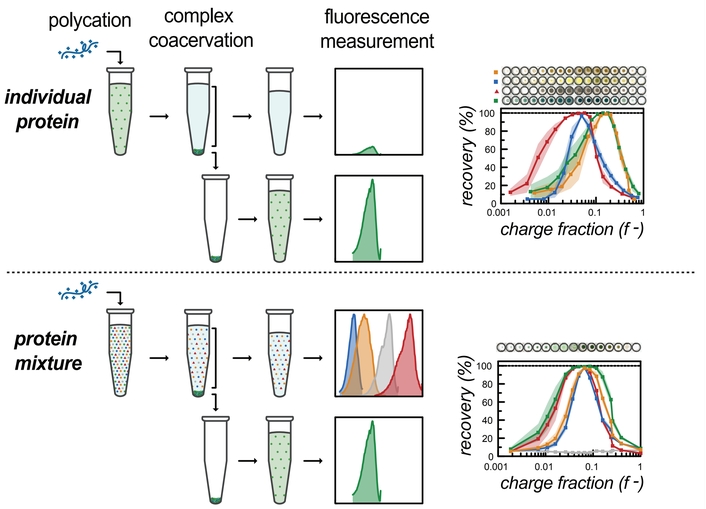

Sustainable Materials

engineering function into bacterial nanocellulose

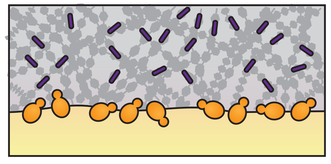

bacteria (*A. xylinum*) produces nanocellulose

engineered yeast secretes nutrients for bacteria produces proteins for functionalization

Acknowledgements

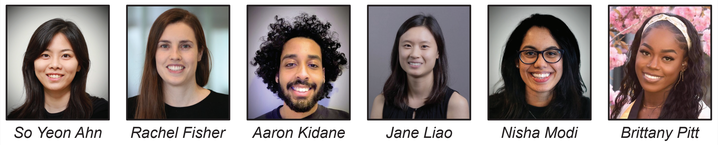

Undergraduate and Masters Students:
Imelda Adjei, Olive Cheng, Lavinia Goessling, Max Kearns, Filimon Keleta, Eun Sol Kim, Jacob Rosenfeld

Protein & Metabolic Engineering

Dr. Scott Banta

Current PhD Students: Mallori Herishko, Wei Wang, Farid Khoury, Ipek Simay Gokulu, and Salomon Vainstein

Engineering Proteins for Selective Recovery of REEs

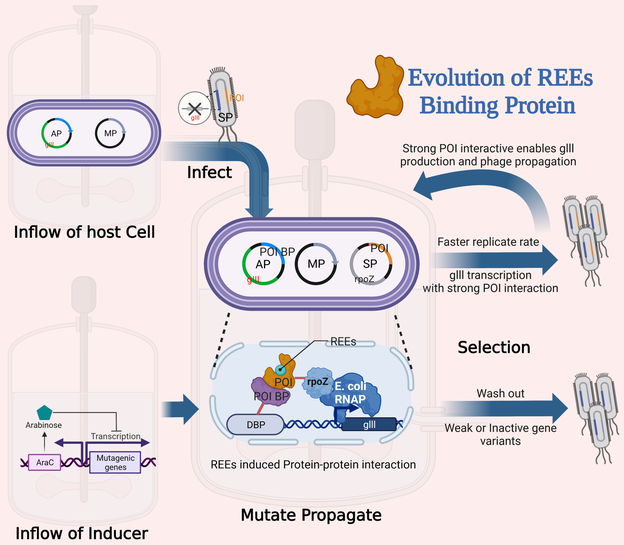

Biofilm Formation Cycle of Acidophilic Bacteria for Bioprocessing Applications

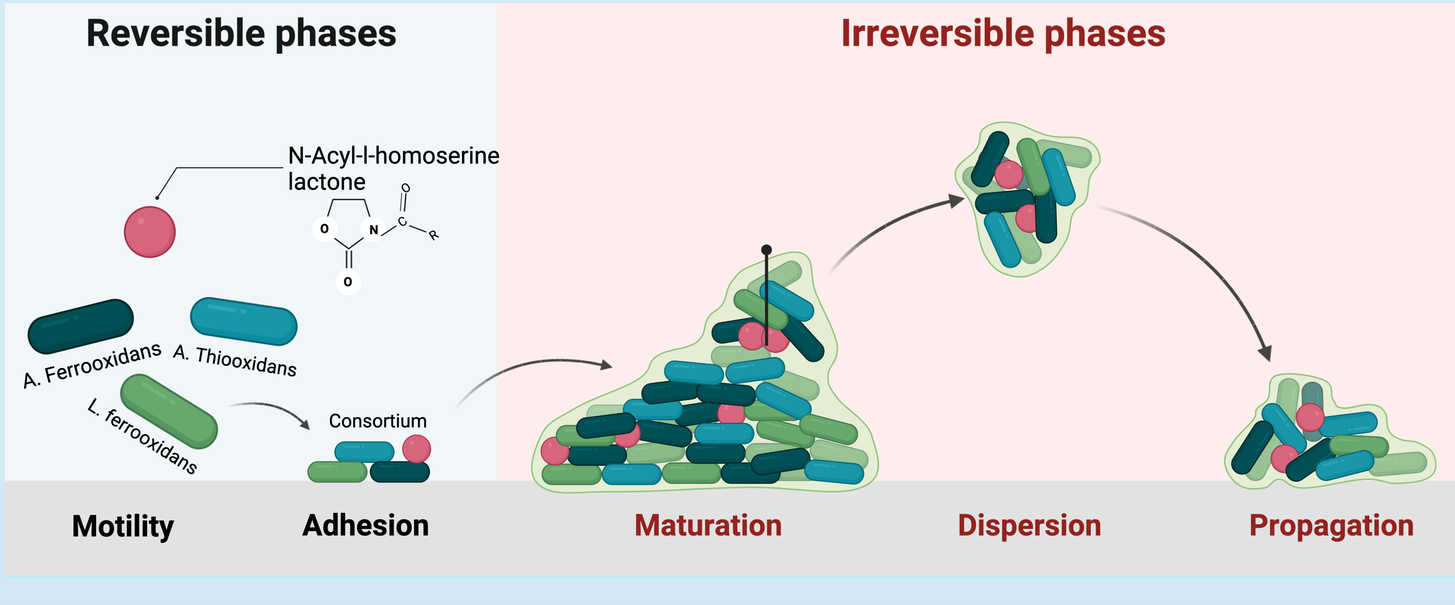

Calcium-dependent Protein Purification Platform

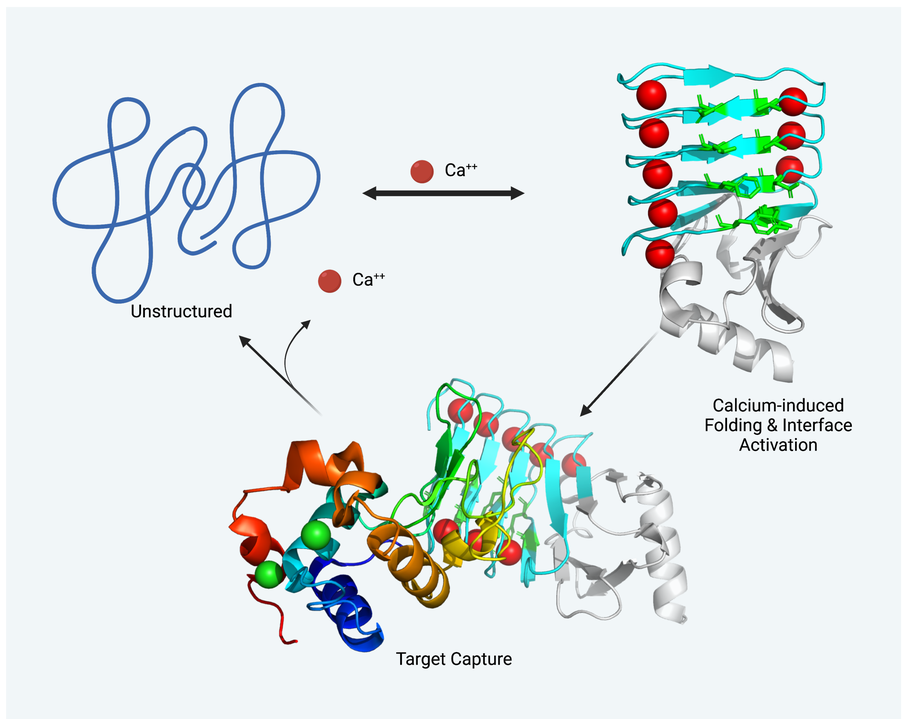

DNA Springs Altering Enzymes Activity

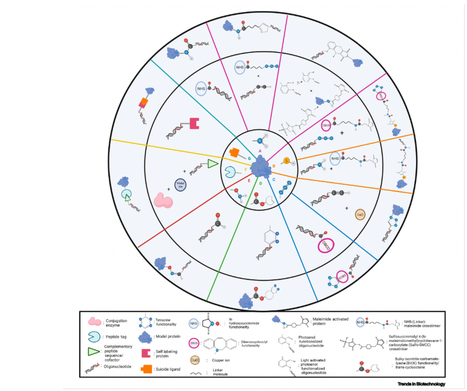

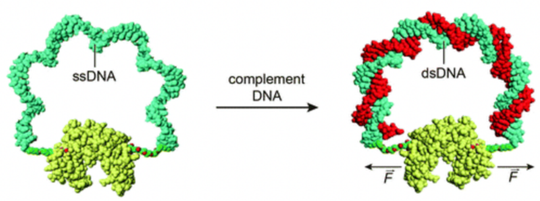

Enzymes with Non-Canonical Cofactors

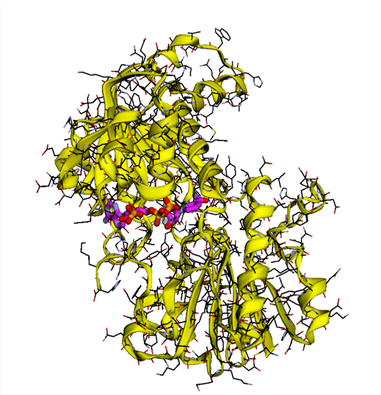

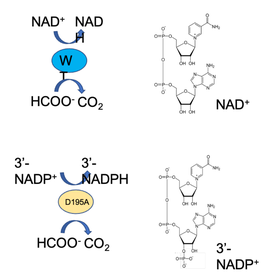

Bio-Inspired SyntHetic sOft matter grouP

Bishop Research Group

Dynamic functions in living matter

Living materials and machines perform *dynamic* functions.

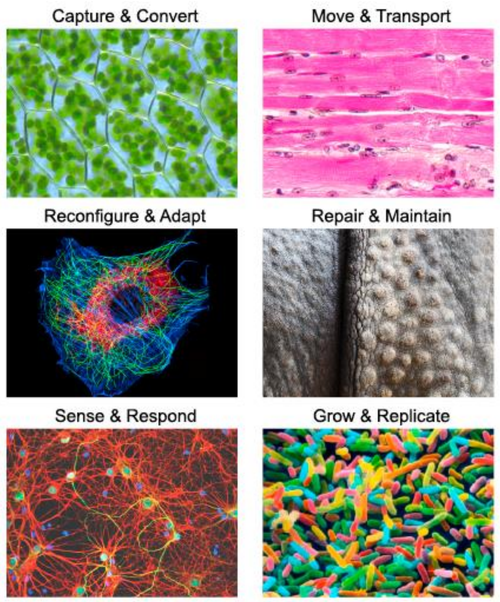

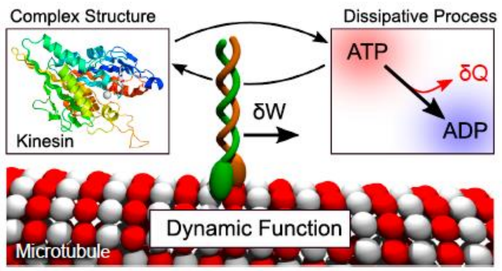

Dynamic functions require the coupling of **complex structures** and **dissipative processes**

Dynamic functions in synthetic active matter

Complex Structures

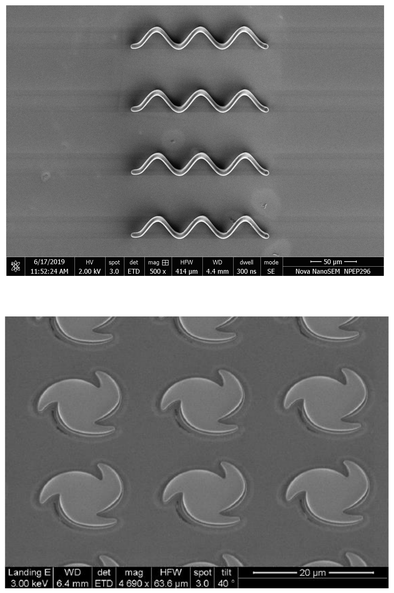

Dissipative Process

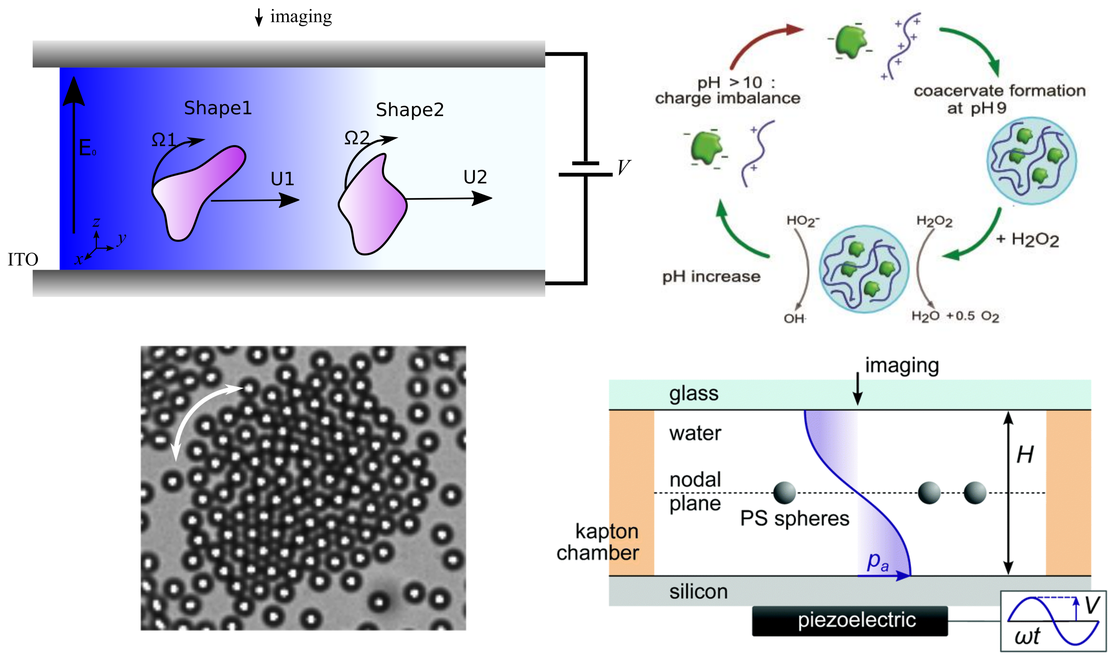

Optimal Design

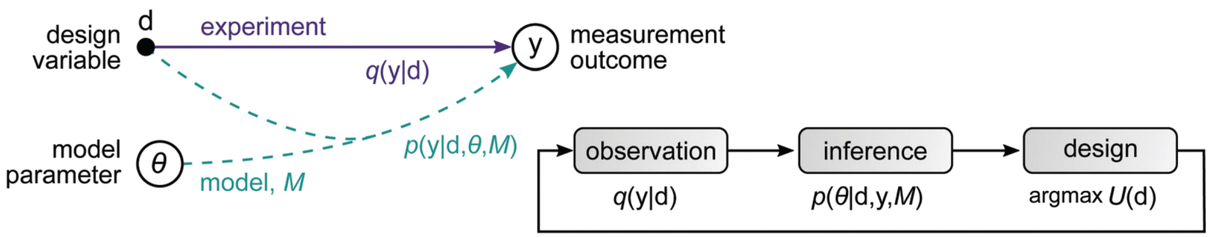

Motion

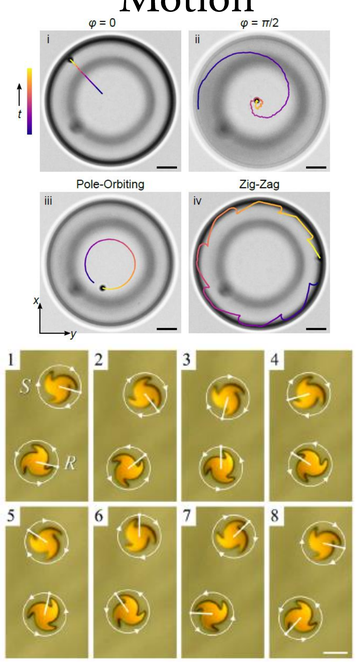

Self Organization

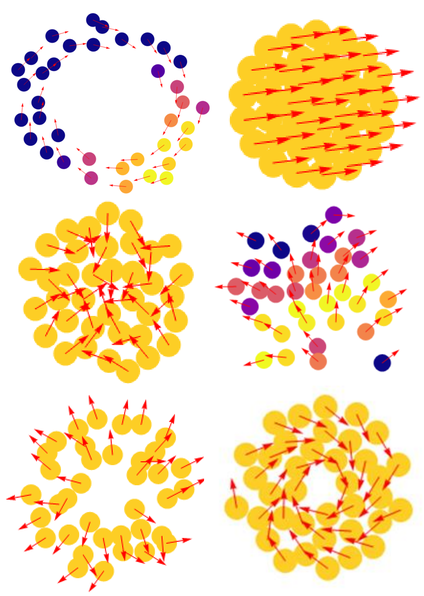

Navigation

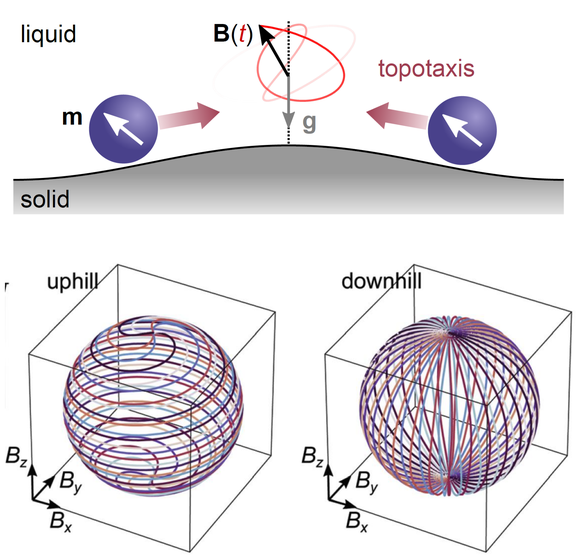

Center for Bio-Inspired Energy Science

U.S. DEPARTMENT OF ENERGY

Boyce Group

Characterizing and Structuring Complex Flows

Applications

Sustainable Mining

Filtration

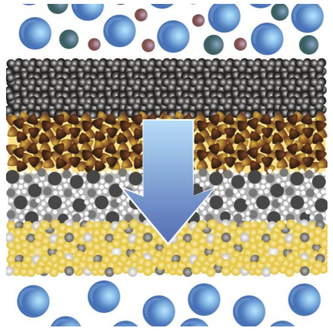

Hydrogen Production

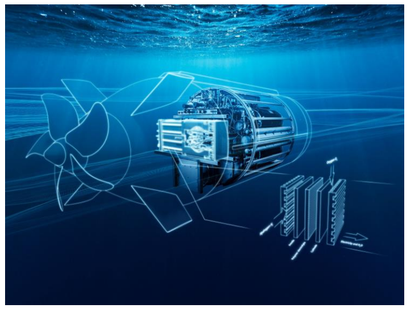

Pharmaceutical Mixing

Techniques

Magnetic Resonance Imaging (MRI) of Flow

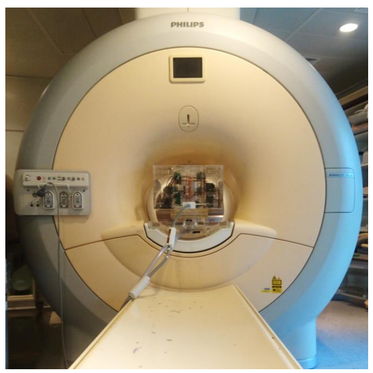

Optical Imaging

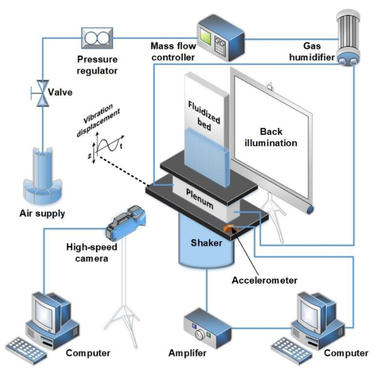

Computational Modeling

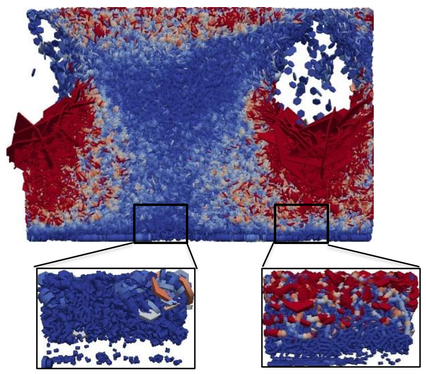

Structured Complex Flows

Granular Flows Subject to Gas Flow and Vibration

Structured Bubbling

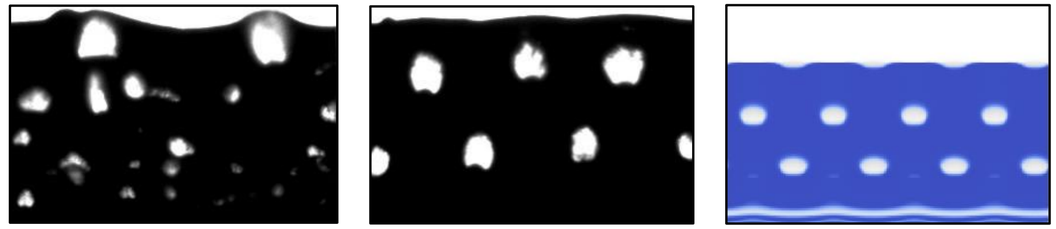

Faraday Waves

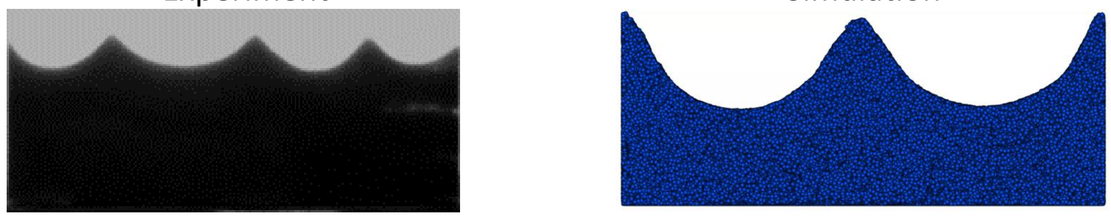

Rayleigh-Bénard Convection

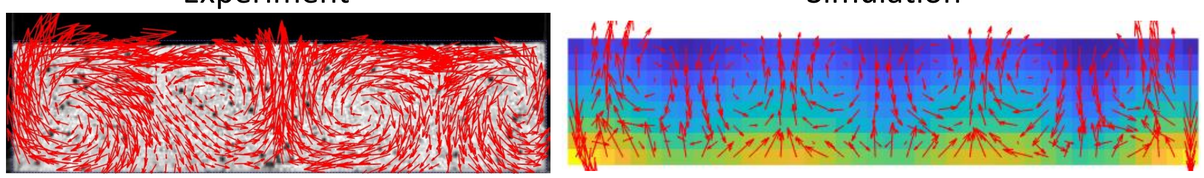

Dense Suspensions

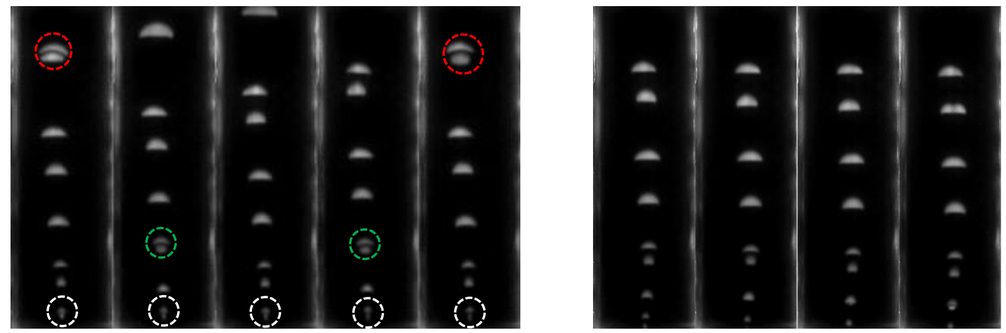

Journals in which we Publish: **General Science:** PNAS; **Fluid Mechanics:** Physical Review Fluids; **Chemical Engineering:** AIChE J., Chem. Eng. Sci., Ind. Eng. Chem Res.

COLUMBIA | ENGINEERING
The Fu Foundation School of Engineering and Applied Science

Recent Research in the Chen Group

COLUMBIA ENGINEERING FOR HUMANITY

Surface Science

Combining model surfaces with supported catalysts

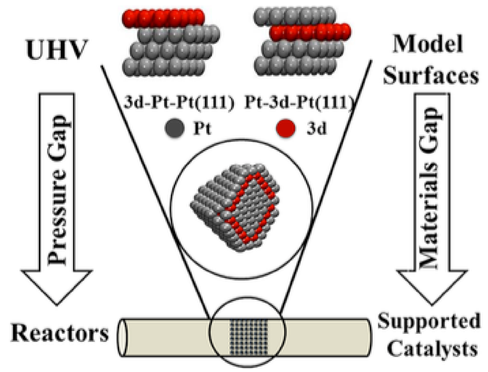

Single Crystal Model Surfaces
- DFT Modelling
- ML predictions
- UHV studies

→ **Bridging the Materials Gap**
- Thin Films
- Supported Catalysts
- Bimetallic catalysts

→ **Bridging the Pressure Gap**
- Flow reactor studies
- Electrocheimcal cells

- ***Single crystals and model surfaces*** are used to gain a fundamental, atomic-level understanding through a combination of experiments and theory
- ***Supported catalysts and bimetallic catalysts*** are more relevant to industrial catalysts and commercial processes
- DFT calculations and in-situ characterizations provide in-depth understanding of active sites and reaction mechanisms

Transition metal carbides and nitrides

- Forming carbides and nitrides from earth-abundant transition metals leads to enhanced activity, selectivity, and stability
- Earth-abundant metals are more attractive due to lower costs, lower scarcity, and lessened environmental impact compared to platinum group metals
- TMNs and TMCs can be used as catalyts themselves or used as active support materials for a primary catalyst metal

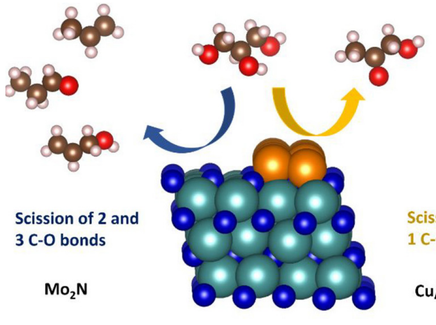

- Mo_2N and Cu/Mo_2N catalyzed selective scission of C-O bonds in glycerol to produce value-added chemicals
- DFT Calculations revealed key active sites and reaction mechanisms

Electrocatalysis

Transition metal carbide-supported Platinum for Glycerol Electrooxidation

- Pt and TMCs exhibit synergystic catalytic effects
- Pt/TaC and Pt/WC demonstrated enhanced C-C bond scission in glycerol
- DFT calculations point to more favorable glycerol adsorption and reduced CO poisoning

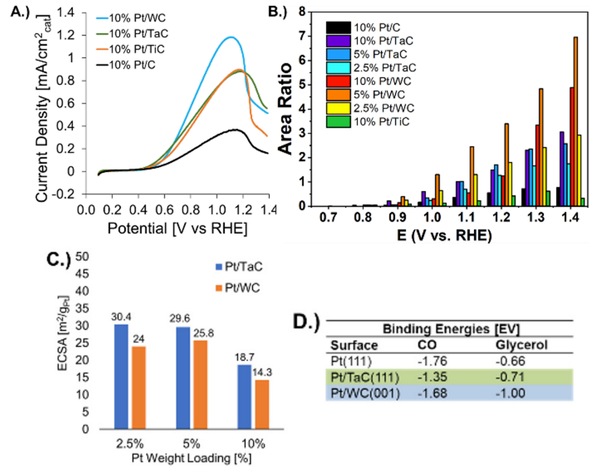

D.)

Binding Energies [EV]		
Surface	CO	Glycerol
Pt(111)	-1.76	-0.66
Pt/TaC(111)	-1.35	-0.71
Pt/WC(001)	-1.68	-1.00

Figure 1. A.) 20th positive CV sweep of 10 wt% Pt/WC, 10 wt% Pt/TaC, 10 wt% Pt/TiC, and 10 wt% Pt/C, normalized by ECSA; B.) ECSA values for 2.5 wt%, 5 wt%, and 10 wt% Pt/TaC and Pt/WC; C.) Peak area ratios of CO_2/carboxylic acid from in-situ FTIR data; D.) CO and glycerol binding energies from DFT calculations

Electrochemical Syngas production from CO_2 using Pd-modified TMNs and TMCs

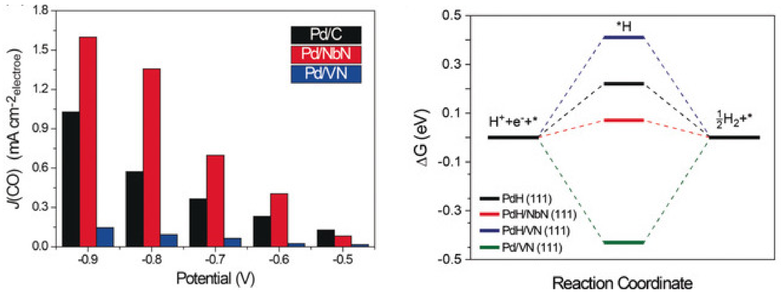

- Forming carbides and nitrides from earth-abundant transition metals leads to enhanced activity, selectivity, and stability
- Earth-abundant metals are more attractive due to lower costs, lower scarcity, and lessened environmental impact compared to platinum group metals
- TMNs and TMCs can be used as catalyts themselves or used as active support materials for a primary catalyst metal

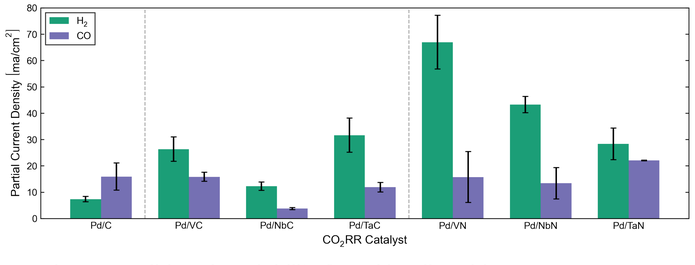

- MEA experiments validated scalability from H-cell architecture
- 5-fold increase in total current density relative to Pd/C
- Choice of TMN support can change CO:H_2 ratio

Tandem Catalysis and Integrated Reactors

- Electrochemical CO_2 reduction has several significant barriers to real-world implementation:
  - Low selectivity for multicarbon (C_{2+}) products
  - Low single-pass CO_2 conversion
  - Low production rates of complex products such as oxygenates and aromatics
- Mixtures of simple CO_2RR products (H_2, CO, C_2H_4) are inputs to many well-understood thermocatalytic reactions
- Complex products can be synthesized directly from CO_2 by implementing a thermochemical reactor downstream of an electrochemical reactor

Integrated reactors for producing C_3 oxygenates

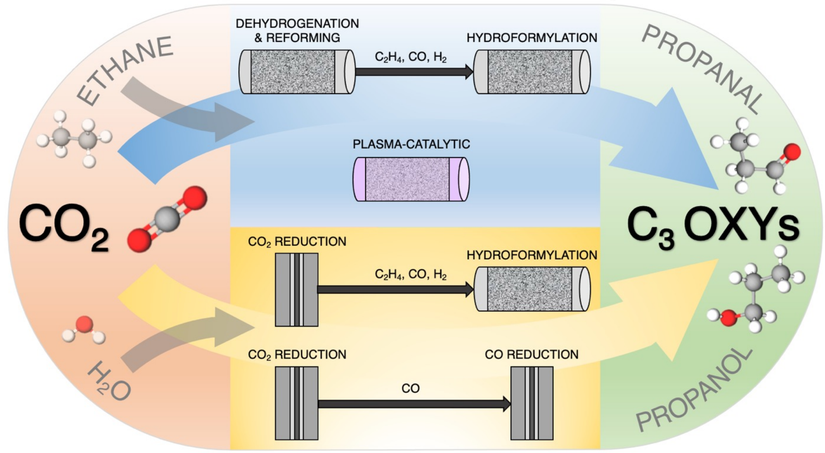

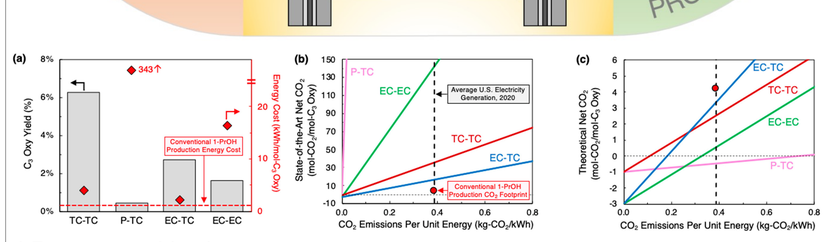

4 Reactor combinations:
- Thermocatalytic-Thermocatalytic (TC-TC)
- Electrocatalytic-Electrocatalytic (EC-EC)
- Electrocatalytic-Thermocatalytic (EC-TC)
- Plasma-Thermocatalytic (P-TC)

Integrated reactors for BTEX Synthesis

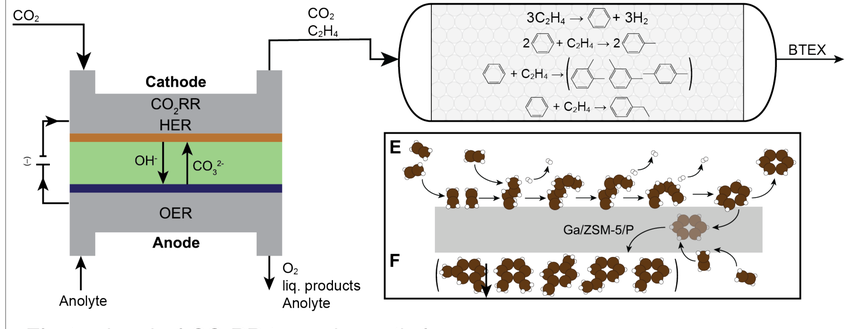

- Electrochemical CO_2RR to produce ethylene
- Thermochemical ethylene aromatization using Ga/ZSM-5/P catalyst to produce BTEX (benzene, toluene, ethylbenzene, xylenes)
- Unreacted CO2 can consume deposited carbon via the reverse Boudouard reaction

Combining Domain Knowledge with Artificial Intelligence for Model Discovery, Drug Discovery and Manufacturing, and Emergence

Vipul Mann, Arijit Chakraborty, Arun Sankar, and Venkat Venkatasubramanian*

CRIS Lab, Department of Chemical Engineering, Columbia University

COLUMBIA | ENGINEERING
The Fu Foundation School of Engineering and Applied Science
COMPLEX RESILIENT INTELLIGENT SYSTEMS

Model Discovery

Automated Modeling Knowledge Extraction

- Given a book, detect mathematical models, and corresponding contextual information
- Automatically populate an ontology with knowledge extracted

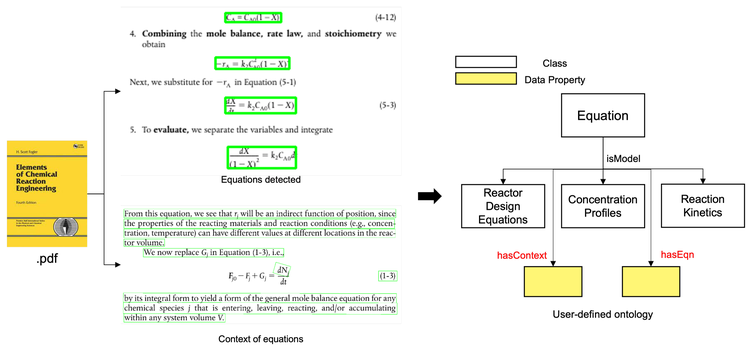

Figure 1: Knowledge extraction algorithm

Data-driven Model Discovery

- Given data, discover underlying mechanistic model(s)
- Incorporate **first-principles** knowledge into **data-driven** modeling $\longrightarrow$ **Hybrid AI** systems (Chakraborty et al., 2021)

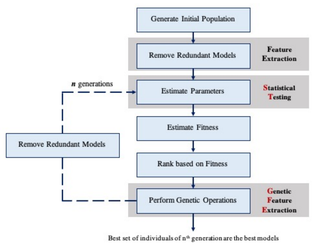

Figure 2: AI-DARWIN algorithm

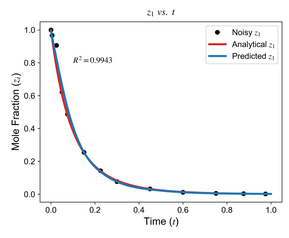

Figure 3: Model performance

XAI-MEG: Explainable AI for mechanistic explanation generation

(Sivaram and Venkatasubramanian, 2021)

- **Symbolic AI + Machine Learning**
- Features and symbolic interpretation used to make model
- Parameters + Model form $\rightarrow$ **Explanations**
  - Causal Graphs
  - Phenomenon tagging
  - Natural language explanations

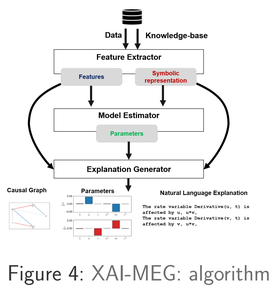

Figure 4: XAI-MEG: algorithm

Drug Discovery and Manufacturing

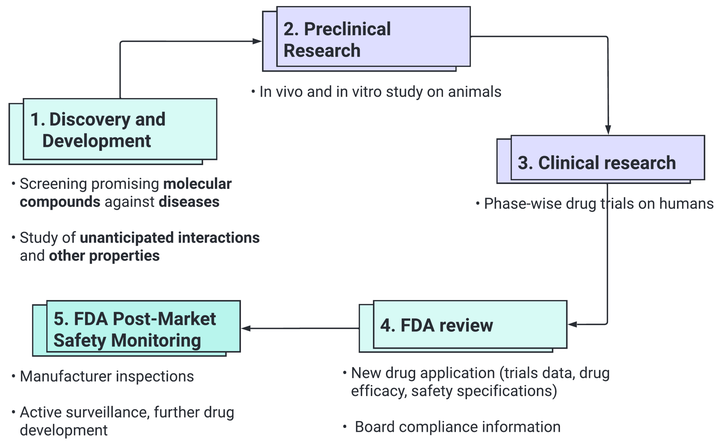

Figure 5: The drug discovery and development cycle

Accelerate the drug discovery and development cycle utilizing domain knowledge (chemicals, diseases, clinical terms) with AI methods

- **Stage 1:** Discovery and development: screening, property prediction Mann et al. (2022)
- **Stage 4:** FDA review: text-processing, information extraction
- **Stage 5:** Safety monitoring: site inspections, risk assessment

A. Information extraction for drug discovery from **unstructured text**:

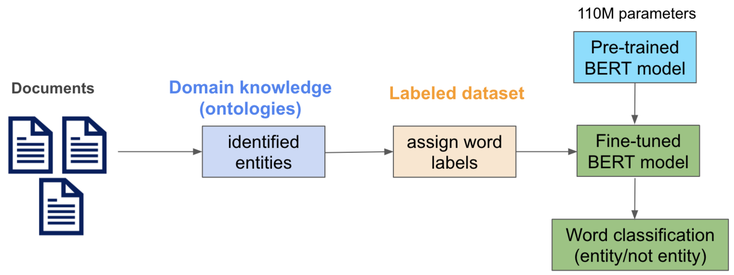

Figure 6: Information extraction from (un)structured text documents

Ontology: formal specification of domain knowledge; class-subclass hierarchy and properties $\longrightarrow$ *knowledge graph*
Named Entity Recognition: 'entities of interest' from unstructured text
BERT model: NLP-based sequence model for language modeling

B. Manufacturing site risk assessment from **regulatory inspections**:

- Modeling site inspection results using text-based models to assess risk level
- Identify subjectivity and human bias in regulatory inspections

Emergence

Figure 7: The axisymmetric nature of ant craters

- Active systems of bacteria, ants and even people can be seen as *goal-driven* systems
- Domain of non-equilibrium statistical physics, one can *still* identify a utility function to establish the formation of patterns in these systems
- Each agent tries to maximize their *utility* (h_i) – goal – in the process attains equilibrium distribution
- **Statistical Teleodynamics** – *Telos* means Goal

System	Utility
Thermodynamic Game	$-\beta E_i - \ln N_i$
Pay Game	$\alpha \ln S_i - \beta(\ln S_i)^2 - \gamma \ln N_i$
Chemotaxis Game	$\alpha c_i - \ln N_i$
Ant crater formation	$b - \frac{\omega r_i^a}{a} - \ln N_i$
Schelling Game	$\eta N_i - \xi N_i^2 + \ln(H - N_i) - \ln N_i$

- Thermodynamic game – Boltzmann distribution
- Pay game – Log-normal distribution
- Chemotaxis game – higher concentration of agents in more food zones
- Ant crater formation – Weibull distribution
- Schelling Game – Shows phase segregation

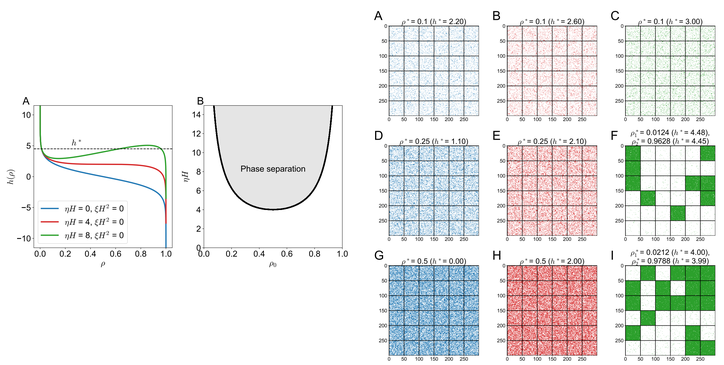

Figure 8: Segregation in Schelling system – Utility function and phase segregation

References

Arijit Chakraborty, Abhishek Sivaram, and Venkat Venkatasubramanian. Ai-darwin: A first principles-based model discovery engine using machine learning. *Computers & Chemical Engineering*, 154:107470, 2021.

Vipul Mann, Karoline Brito, Rafiqul Gani, and Venkat Venkatasubramanian. Hybrid, interpretable machine learning for thermodynamic property estimation using grammar2vec for molecular representation. *Fluid Phase Equilibria*, 561:113531, 2022.

Abhishek Sivaram and Venkat Venkatasubramanian. XAI-MEG: Combining symbolic AI and machine learning to generate first-principles models and causal explanations. *AIChE Journal*, page e17687, 2021.

Combination of Antiviral Drugs to Inhibit SARS-CoV-2 Polymerase and Exonuclease as COVID-19 Therapeutics

Doris Yue[1,2], Kao Lin[1,2], Xiaoxu Li[1,2], Chuanjuan Tao[1,2], Shiv Kumar[1,2], Xuanting Wang [1,2], Steffen Jockusch [1,5], Irina Morozova [1,2], Sergey Kalachikov [1,2], Minchen Chien[1,2], Carolina Q. Sacramento[3,4], Otávio A. Chaves [3,4], Natalia Fintelman-Rodrigues[3,4], Jairo R. Temerozo [6,7], Wei Xie[8], Dinshaw J. Patel [8], Thomas Tuschl[9],Patrícia T. Bozza [3], Thiago Moreno L. Souza [3,4] James J. Russo[1,2], & Jingyue Ju [1,2,10]

1 Center for Genome Technology and Biomolecular Engineering, Columbia University, New York, NY 10027, USA. 2 Department of Chemical Engineering, Columbia University, New York, NY 10027, USA. 3 Laboratory of Immunopharmacology, Oswaldo Cruz Institute (IOC), Oswaldo Cruz Foundation (Fiocruz), Rio de Janeiro, RJ, Brazil. 4 National Institute for Science and Technology for Innovation on Diseases of Neglected Population (INCT/IDPN), Center for Technological Development in Health (CDTS), Oswaldo Cruz Foundation (Fiocruz), Rio de Janeiro, RJ, Brazil. 5 Department of Chemistry, Columbia University, New York, NY 10027, USA. 6 Laboratory on Thymus Research, Oswaldo Cruz Institute (IOC), Oswaldo Cruz Foundation (Fiocruz), Rio de Janeiro, RJ, Brazil. 7 National Institute for Science and Technology on Neuroimmunomodulation (INCT/NIM), Oswaldo Cruz Institute (IOC), Oswaldo Cruz Foundation (Fiocruz), Rio de Janeiro, RJ, Brazil. 8 Laboratory of Structural Biology, Memorial Sloan-Kettering Cancer Center, New York, NY 10065, USA. 9 Laboratory of RNA Molecular Biology, Rockefeller University, New York, NY 10065, USA. 10 Department of Molecular Pharmacology and Therapeutics, Columbia University, New York, NY 10032, USA.

Background

Coronaviruses Assemble a Multiple Protein Complex to Synthesize their RNA Genomes

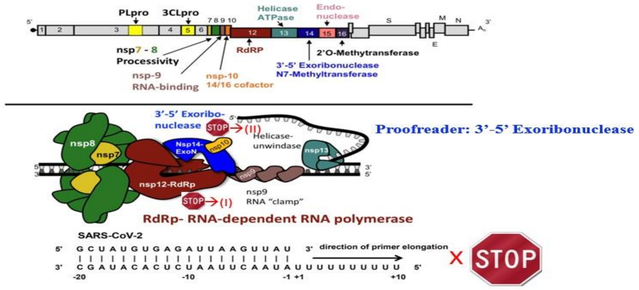

The 30 kb genome of SARS-CoV-2 (top) encodes a host of proteins critical for the virus's life cycle. Many of the non-structural proteins (nsps), including an error-prone RNA-dependent RNA polymerase (RdRp, nsp12), a proof-reading exonuclease (ExoN, nsp14), helicase, and various accessory proteins, assemble to form the replication-transcription complex (middle). During the replication of viral RNAs, nucleotide inhibitors incorporated by RdRp are often subject to removal by ExoN, reducing efficacy of these drugs for treating COVID-19. We reason that combinations of inhibitors of both (RdRp) and exonuclease (ExoN) can overcome this deficiency.

We showed that the hepatitis C virus NS5A inhibitors Pibrentasvir and Ombitasvir are ExoN inhibitors. In the presence of Pibrentasvir, RNAs terminated with active forms of Sofosbuvir, Remdesivir, Favipiravir, Molnupiravir and AT-527 prodrugs were largely protected from excision by ExoN; in the absence of Pibrentasvir, there was rapid excision. Due to its unique structure, Tenofovir-terminated RNA was highly resistant to ExoN excision even in the absence of Pibrentasvir. Viral cell culture studies demonstrate significant synergy of virus inhibition using a combination of SARS-CoV-2 RdRp inhibitors (*e.g.*, Remdesivir and Favipiravir) and ExoN inhibitors (*e.g.*, Pibrentasvir and Ombitasvir). This study supports the use of combination drugs that inhibit both the SARS-CoV-2 polymerase and exonuclease for effective COVID-19 treatment.

Active Forms of Prodrugs Used in this Study

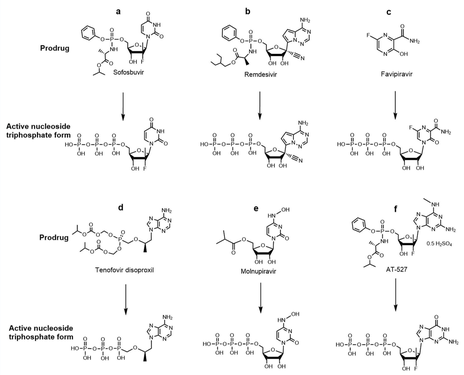

Fig. 1: Prodrugs of polymerase inhibitors and their active triphosphate forms. Structures of the prodrugs Sofosbuvir (a), Remdesivir (b), Favipiravir (c), Tenofovir disoproxil (d), Molnupiravir (e), and AT-527 (f) (top) and their respective active triphosphate forms Sofosbuvir-5'-triphosphate, Remdesivir-5'-triphosphate, Favipiravir ribofuranosyl-5'-triphosphate (Favipiravir-RTP), Tenofovir diphosphate, N4-hydroxycytidine-5'-triphosphate (NHC-TP), and 2'-fluoro-2'-methyl guanosine-5'-triphosphate (AT-9010, Gfm-TP) (bottom). We and others have previously shown that each of these nucleotide analogs can be incorporated into RNA by the SARS-CoV-2 RdRp, where they either halt further RNA extension or display mutagenic potential.

Inhibition of SARS-CoV-2 Exonuclease by HCV NS5A Inhibitors Ombitasvir and Pibrentasvir

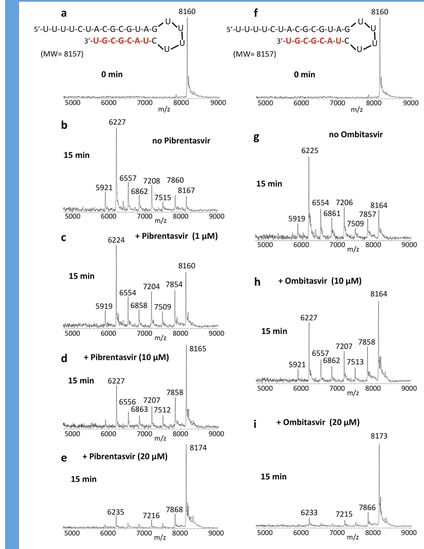

Fig. 3: Inhibition of SARS-CoV-2 ExoN activity by Pibrentasvir and Ombitasvir. Mixtures of RNA (sequence at top) and SARS-CoV-2 ExoN complex (nsp14/nsp10) were incubated in the absence (b, g) and presence of Pibrentasvir (c–e) or Ombitasvir (h, i) followed by MALDI-TOF MS analysis. In the absence of Pibrentasvir, ExoN cleaves nucleotides from the RNA 3'-end (7 lower molecular weight fragments) with ~7% intact RNA (8160 Da peak) remaining (b). Increasing Pibrentasvir lowers ExoN activity, as shown by reduced fragmentation peaks and more intact RNA (c–e). Ombitasvir gives similar results (f–i).

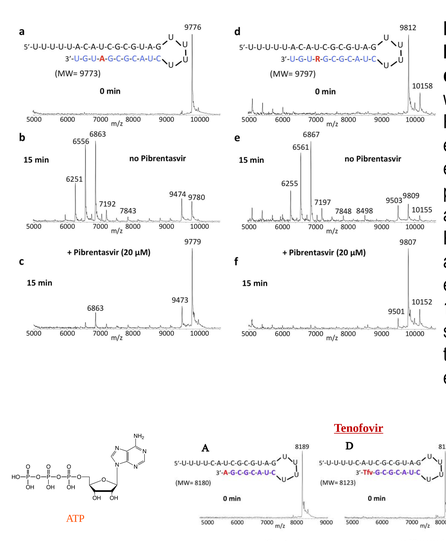

Fig. 4: Inhibition of SARS-CoV-2 ExoN activity by Pibrentasvir for natural RNA and RNA with delayed termination by Remdesivir (R). RNA was designed to mimic delayed termination by Remdesivir (R positioned 4 bases from the 3' end; delayed termination that evades exonuclease excision is the mechanism previously proposed for Remdesivir's antiviral activity. However, we found that in the absence of Pibrentasvir, ExoN cleavage from the 3' end (e) is as efficient as with natural RNA (b), which might explain Remdesivir's lower efficacy for COVID-19. With Pibrentasvir present, ExoN activity is significantly reduced for Remdesivr delayed terminated RNA (f) which should increase the efficacy of this drug combination for COVID-19.

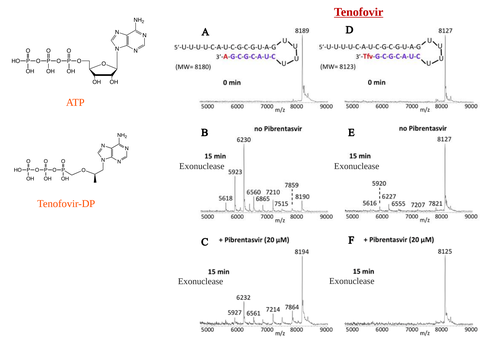

Fig. 5: Tenofovir (Tfv) terminated RNA has significant resistance to SARS-CoV-2 ExoN activity. Tfv terminated RNA is less likely to be cleaved by ExoN even in the absence of Pibrentasvir (e) relative to natural RNA (b), as evidenced by the significant diminution in fragment peaks. We have reasoned that Tfv's acyclic structure is likely to interfere with exonuclease recognition. Even further inhibition of ExoN cleavage occurred in the presence of Pibrentasvir (f) relative to natural RNA (c), where the Tfv terminated RNA is almost completely protected.

Potential Binding of Inhibitors to Exonuclease

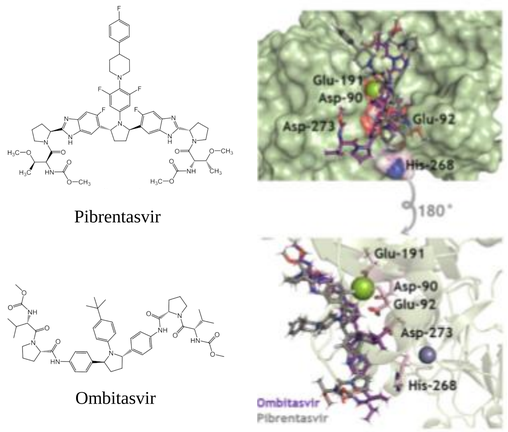

Fig. 2: Identification of HCV drugs Pibrentasvir and Ombitasvir as SARS-CoV-2 exonuclease inhibitors. 3D representation of best docking poses for the two drugs in the nsp14 exonuclease active site. Docking was performed using GOLD 2020.2 software with ChemPLP scoring function. Inhibitor and catalytic amino acid residues in stick representation. Mg^{++} and Zn^{++} represented as green and indigo spheres, respectively.

Based on modeling, these inhibitors interfere with the coordination among the Mg^{++} ion, the essential Asp and Glu amino acids in the nsp14 active site and the RNA 3' terminus, which likely prevents nucleotide excision from the RNA.

Combination of Polymerase and Exonuclease Inhibitors Enhances SARS-CoV-2 Inhibition in Cell Culture

	Antiviral Drug	EC_{50}* Mean	EC_{50}* SEM**
Identified SARS-CoV-2 Exonuclease inhibitors	Pibrentasvir	0.7	0.2
	Ombitasvir	0.4	0.05
	Daclatasvir	0.7	0.08
RdRp inhibitor	Remdesivir (RDV)	0.09	0.002
RdRp + Exonuclease inhibitors	RDV + Pibrentasvir (0.1μM)	0.008	0.0009
	RDV + Ombitasvir (0.1μM)	0.008	0.0003
	RDV + Daclatasvir (0.5μM)	0.008	0.0006
	Favipiravir	7.8	1.2
	Favipiravir + Ombitasvir (0.1μM)	0.15	0.04
	Favipiravir + Pibrentasvir (0.1μM)	0.5	0.03
	Favipiravir + Daclatasvir (0.5μM)	0.12	0.05
	Tenofovir	4.3	2.1
	Tenofovir + Pibrentasvir (0.1μM)	0.5	0.05
	Tenofovir + Ombitasvir (0.1μM)	0.8	0.07
	Tenofovir + Daclatasvir (0.5μM)	0.01	0.004

*: Half maximal effective concentration of a drug (inhibited the virus production by 50%)
**: Standard Error of the Mean

Antiviral activity of combinations of SARS-CoV-2 polymerase (RdRp) and exonuclease inhibitors. Our collaborator Dr. Souza's group performed virus inhibitory experiments with combinations of RdRp and exonuclease inhibitors. Calu-3 cells were infected with SARS-CoV-2 and after washing, cells were incubated with the indicated concentration of Remdesivir (RDV), Sofosbuvir, Tenofovir and Favipiravir, alone and in combination with the EC_{25} concentrations of HCV NS5A inhibitors Pibrentasvir (0.1 μM), Ombitasvir (0.1 μM) and Daclatasvir (0.5 μM). After 2-3 days, viral replication in the culture supernatant was measured as PFU/mL by titering Vero E6 cells. Representative data are presented in the table.

The combination of the ExoN inhibitor Pibrentasvir with the RdRp inhibitor Remdesivir can increase RDV's potency 10-fold. When Favipiravir mixed with ExoN inhibitors such as Ombitasvir, its potency is increased over 50-fold. This *in vitro* data agrees with our enzymatic results demonstrating that the SARS-CoV-2 susceptibility to inhibition by nucleotide analogues can be enhanced with exonuclease inhibitors.

Degree of Resistance to Exonuclease Excision by Different Nucleotide Analogs

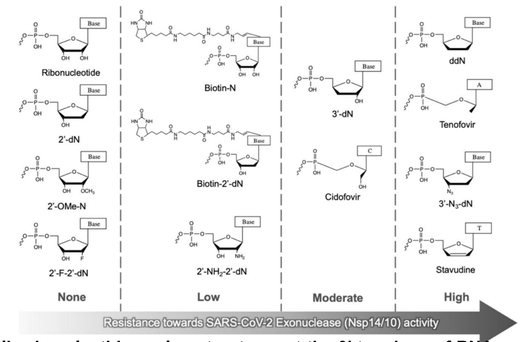

Summary of generalized nucleotide analog structures at the 3' terminus of RNA organized based on their resistance towards SARS-CoV-2 exonuclease activity. A library of RNAs each containing a distinct nucleotide at its 3' end was prepared by chemical synthesis or polymerase extension. After incubation with SARS-CoV-2 ExoN and use of MALDI-TOF MS to reveal cleavage, results indicated that these nucleotide analogs fall into 4 groups showing increasing resistance to ExoN excision from left to right, where N indicates any tested nucleobase. These findings suggest nucleotide analog inhibitor designs that may provide both efficient incorporation by SARS-CoV-2 RdRp and at the same time resist ExoN activity, yielding potential lead compounds for treating COVID-19 and related viral infections.

References & Acknowledgements

Wang X. et al. *Commun Biol.* **2022**, 1, 154.
Ju J et al. *Pharmacol Res Perspect* **2020**, 8, e00674.
Jockusch S et al. *Antiviral Res* **2020**, 180, 104857.
Wang X et al. *Viruses*. **2022**, 14, 1413.
Jockusch S. et al. *Sci Rep* **2020**, 10, 16577.
Chien M. et al. *J Proteome Res* **2020**, 19, 4690.

Work at Columbia was supported by Jack Ma Foundation, a gift from Columbia Engineering Member of the Board of Visitors Dr. Bing Zhao, Fast Grants, and NIH/NIAID grant 1U19AI171401-01.

Single-Molecule Electronic DNA Sequencing-By-Synthesis using Tagged Nucleotides and Nanopore Detection

Shiv Kumar [1], Sergey Kalachikov [1], Xiaoxu Li [1], Xuanting Wang [1], Irina Morozova [1], Chuanjuan Tao [1], James J. Russo [1], John J. Kasianowicz [2], Sukanya Punthambaker [3], George M. Church [3], *Jingyue Ju* [1]

[1] Center for Genome Technology and Biomolecular Engineering, Departments of Chemical Engineering and Pharmacology, Columbia University, New York, NY 10027

[2] National Institute of Standards and Technology, Gaithersburg, MD 20899;

[3] Department of Genetics, Harvard University, Boston, MA 02115

Abstract

The nanopore-based sequencing by synthesis strategy (Nanopore-SBS) distinguishes DNA bases by electronically detecting different polymer tags attached to nucleotides during their incorporation by DNA polymerase. When an incoming complementary tagged nucleotide forms a ternary complex with primed template and polymerase, the polymer tag enters the pore and produces a unique electrical current blockade level.

Further development focuses on increasing accuracy by introducing the use of high ratios of unincorporable-to-incorporable tagged nucleotides to perform Nanopore-SBS. This approach provides detection of current blockades multiple times due to the 4 unique tags on the unincorporable nucleotides, which display template-dependent binding to the polymerase but are not incorporated into the growing strand, followed by a new current level due to a 5th tag on the incorporable nucleotide that marks the transition to the extension step. This method can eliminate insertion/deletion sequence artifacts, especially for DNA homopolymer regions.

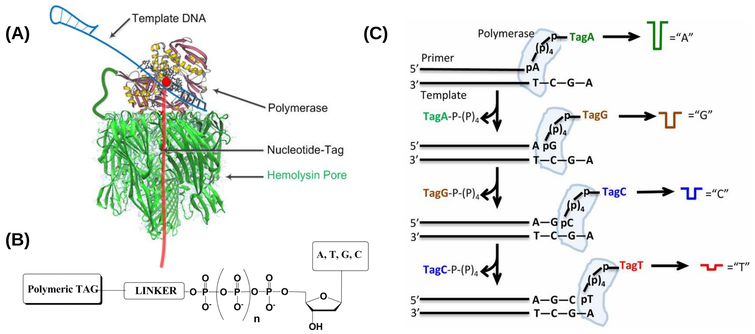

Principle of the Nanopore-SBS sequencing method. (A) A single polymerase molecule covalently attached to the α-hemolysin nanopore heptamer and bound to DNA primer/template and tagged nucleotide during incorporation. (B) Generalized structure of the tagged nucleotides. (C) SBS schematic showing the sequential capture and reading of polymer tags as they are incorporated into the growing primer strand.

Single Molecule Electronic Sequencing by Synthesis (Nanopore-SBS)

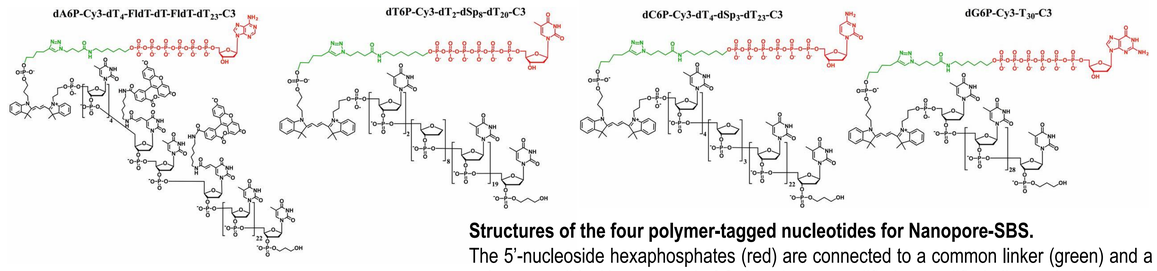

Structures of the four polymer-tagged nucleotides for Nanopore-SBS.
The 5'-nucleoside hexaphosphates (red) are connected to a common linker (green) and a polymer tag (black) composed of Cy3 and an unmodified or modified oligonucleotide.

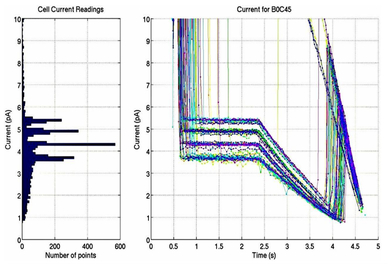

Oligo Tag	Sequence	Tag Current Blockage Level (pA)
dSp_8	5'-TTTTT TTTTT TTSSS SSSSS TTTTT -Biotin-3'	5.5
dSp_3	5'-TTTTT TTTTT TTTTT SSSTT TTTTT -Biotin-3'	4.9
dT_{30}	5'-TTTTT TTTTT TTTTT TTTTT TTTTT -Biotin-3'	4.4
$FldT_2$	5'-TTTTT TTTTT TTTTT FTFTT TTTTT -Biotin-3'	3.8

Different current blockade levels using αHL pores and biotinylated oligonucleotides bound to streptavidin. (Right) Multiple current measurement time courses are overlaid showing the blockade levels obtained when an oligo tag is held in the pore under a constant applied voltage. (Left) Histogram with 4 well-separated peaks for the 4 tagged oligonucleotides.

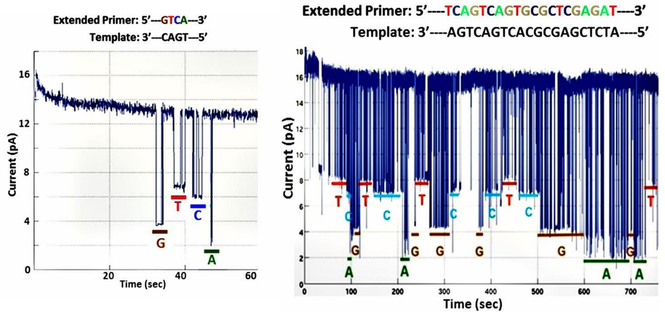

Nanopore-SBS sequencing results on nanopore array chips. (Left) Four nucleobases are clearly distinguished. (Right) A longer sequence read is shown. The nucleotide tag appears to be captured several times in succession ("stuttering") before the tag of the next nucleotide in the sequence is observed.

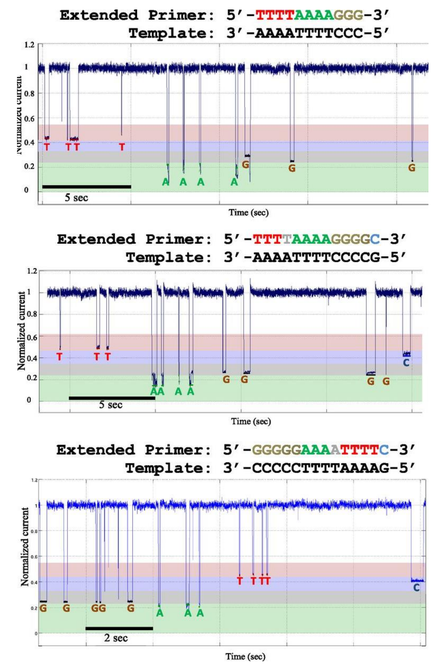

Sequencing results of homopolymer reads. Homopolymer regions were sequenced at relatively high accuracy but some bases were missed (gray). This can be addressed with the use of unincorporable and incorporable tagged nucleotides (see below).

Unincorporable and Incorporable Tagged Nucleotides for High Accuracy Nanopore-SBS

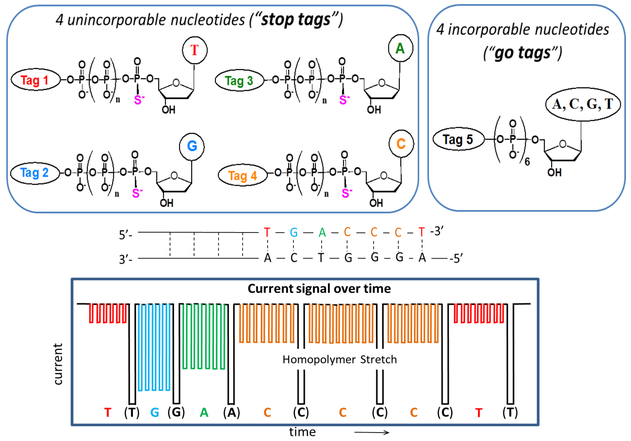

Principle of novel single-molecule electronic Nanopore-SBS approach with use of unincorporable tagged nucleotides and incorporable tagged nucleotides (Stop and Go Nanopore-SBS). As each complementary "stop"-tag nucleotide forms a ternary complex with the polymerase and primed template, a series of signals (bottom) related to each of the 4 tags is obtained ("stutter" signals) for sequence determination. Eventually, the primer is extended with the equivalent "go"-tag nucleotide, producing a lower current signal due to the 5th tag. The intermittent signals produced by the combination of "stop"- and "go"-tag nucleotides is designed to yield highly accurate sequence, and largely eliminate false overcalls and undercalls.

General structures of unincorporable and incorporable tagged nucleotides

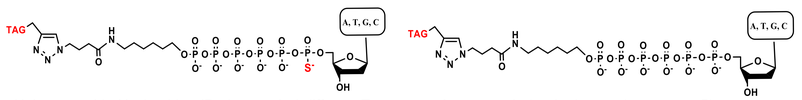

Unincorporable Nucleotides (Rp-isomers): 4 different Tags

dT6P-αS-Cy3-dT_2-dSp_8-dT_{18}-C3
dC6P-αS-Cy3-dT_4-dSp_3-dT_{23}-C3
dG6P-αS-Cy3-dT_{30}-C6
dA6P-αS-Cy3-dT_4-FldT-dT-FldT-dT_{23}-C3

Incorporable Nucleotides with common 5th Tag

5th Tag: Cy3-dT_4-Tmp_8-dT_{18}-C3
or Cy3-dT_2-dSp_{28}-C3

nucleotide	K_D (nM)
dGTP dCTP	6 ~5
dCp-CH_2-pp	25,000
2'-dGTP-αS (Sp-isomer) 2'-dCTP-αS (Sp-isomer)	6 1
2'-dGTP-αS (Rp-isomer) 2'-dCTP-αS (Rp-isomer) αS-dG6P-N_3 (Rp-isomer)	910 750 670

Rp-α-thio-nucleotides are not substrates for DNA polymerase and their K_D is more than 100 fold higher than the natural nucleotides.

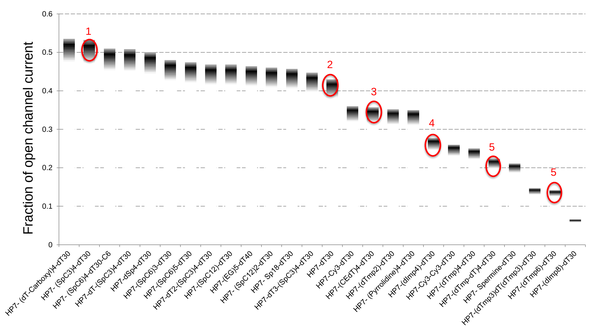

Oligo tags with different features display a wide range of current blockade levels. From these, > 5 oligo tags with distinct signals have been selected to couple to the unincorporable and incorporable nucleoside hexaphosphates.

Synthesis scheme for unincorporable tagged nucleotides

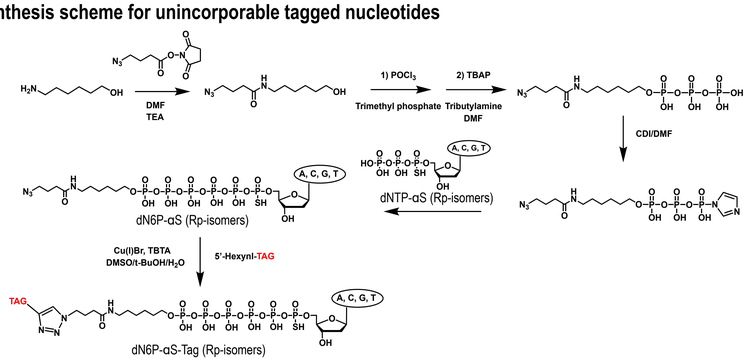

The novel *Stop and Go* Nanopore-SBS approach overcomes the inherent limitation of single-molecule detection methods that only allow one chance for measurement. With the new tagged nucleotides that possess improved properties, better regulated polymerase reaction kinetics, and optimal polymerase-nanopore complexes, we will evaluate the accuracy of the approach by sequencing model templates.

References & Acknowledgements

Kumar, S., & Ju, J. et al. *Sci. Rep.* **2012**, 2, 684.

Fuller, C., Kumar, S., Ju, J. et al. *Proc. Natl. Acad. Sci. (USA)* **2016**, 113, 5233-38.

Stranges, B., Palla, M., Church, M. G. et al. *Proc. Natl. Acad. Sci. (USA)* **2016**, 113, E6749-56.

Palla, M., Punthambaker, S., Church, M. G. et al. *ACS Nano* **2021**, 15, 489-502.

This work has been supported by NIH R01HG010514.

Making Better Batteries: Understanding Degradation and Enhancing Performance in Li and Beyond

Andrew Ells, Julia Hestenes, Bret Schumacher, Yongbeom Kwon, Emily Barragan, Susie Park, Cameron Temple
Naiara Munich, Pablo Buitrago, Lafe Martinson, Lakshmi Bhai, Asya Svirinovsky, and Lauren E. Marbella
Department of Chemical Engineering, Columbia University, New York, NY 10027

Non-invasive quantification of inventory loss in Li metal batteries via *operando* NMR

The use of nuclear magnetic resonance spectroscopy (NMR) while simultaneously cycling a battery allows us to characterize Li deposition morphology in a non-destructive fashion to quantify how much of the Li inventory is lost as electronically isolated Li (dead Li) and Li in the solid electrolyte interphase (SEI). With *operando* ^{7}Li NMR, we found that anode-free batteries that use $LiNi_{0.8}Mn_{0.1}Co_{0.1}O_2$ (NMC811) cathodes are outperformed by those with $LiFePO_4$ (LFP) cathodes, due to high-surface-area plating behavior that exacerbates the production of dead Li over cycles. Using improved electrolyte formulations, such as those with additives, can improve performance by drastically decreasing the build up of dead Li and SEI.

Probing for morphology

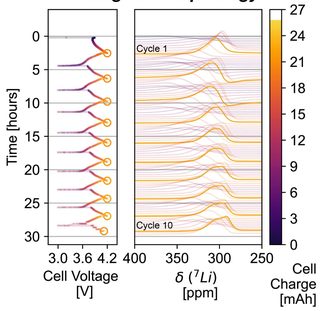

Peak shape evolution indicates morphology change

SEM imaging

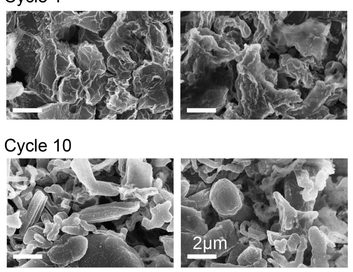

SEM imaging visually confirms increasing Li metal surface area

Quantification of dead Li and SEI buildup

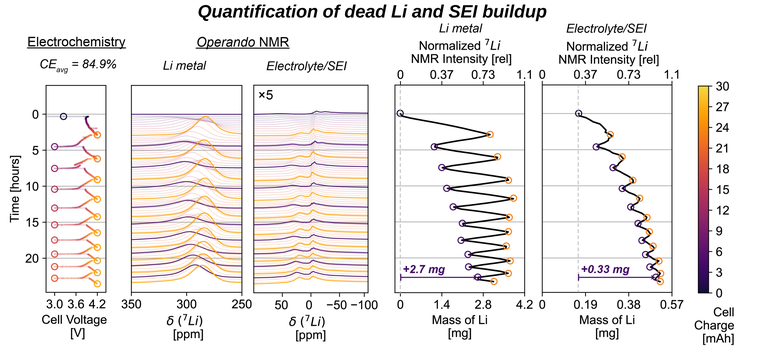

Peak integration allows direct and *in-situ* measurement of the increasing Li losses

Kwon, Y.; Svirinovsky, A.; Corpus, K.; Pecher, O.; Braun, M.; May, R.; Marbella, L.; *in preparation*

Operando NMR/EPR spectroscopies for studying cathode-driven battery degradation

We also use *operando* methods to understand degradation in $LiNi_{0.5}Mn_{1.5}O_4$ (LNMO), a next generation cathode material. *Operando* solution ^{19}F NMR shows that HF forms during cycling and causes transition metal dissolution, as detected by *operando* electron paramagnetic resonance spectroscopy (EPR).

Operando* Battery** ***Battery Charging ***HF formation*** ***Mn dissolution*** ***HF / Mn Quantification***

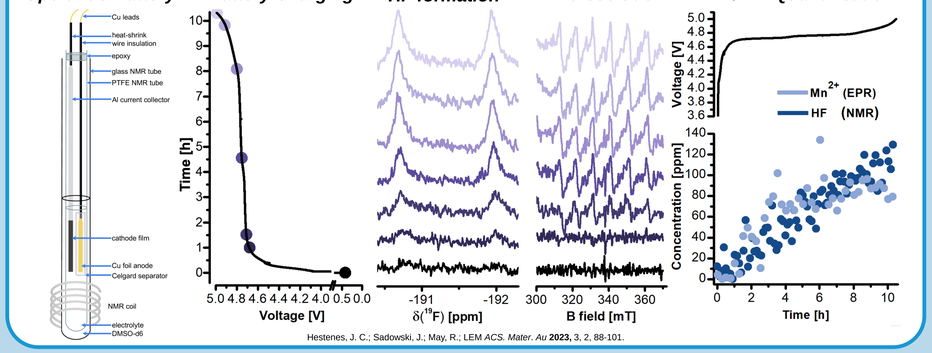

Hestenes, J. C.; Sadowski, J.; May, R.; LEM *ACS. Mater. Au* **2023,** 3, 2, 88-101.

Establishing design rules for K-ion battery electrolytes

K-ion batteries (KIBs) use widely abundant materials and can effectively replace Li-ion batteries (LIBs) for some applications like grid storage. Because KIBs are relatively unexplored, it is not yet understood if they can benefit from the electrolytes we use to optimize LIB performance. For example, fluoroethylene carbonate (FEC) is added to LIB electrolytes to improve their lifetime, but we found that FEC drops the capacity of KIBs immediately. In ^{19}F solid-state NMR, the peak corresponding to KF was only present in FEC electrolytes. This suggests that FEC decomposes to form insoluble KF on the electrode surface, restricting K^+ diffusion into the electrode and dropping capacity (whereas LiF is generally viewed as a favorable decomposition product in LIBs). Our other work in KIBs aims to explain the performance enhancement of other electrolytes, such as those using nonflammable additives.

Assessing battery performance

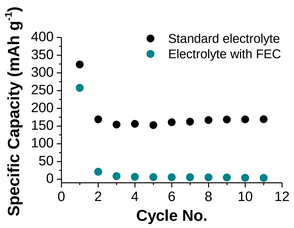

The charge stored in KIBs drops rapidly with FEC electrolyte.

Identifying byproducts of battery operation

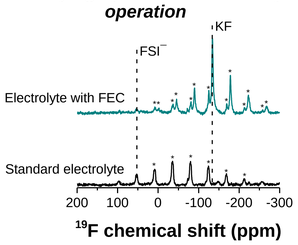

^{19}F NMR shows that KF forms from FEC decomposition.

Connect performance with chemistry

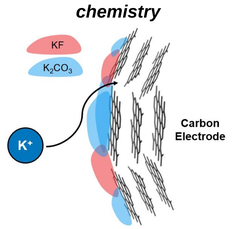

KF on the electrode surface hinders K^+ diffusion and capacity.

Exploring many electrolyte design strategies

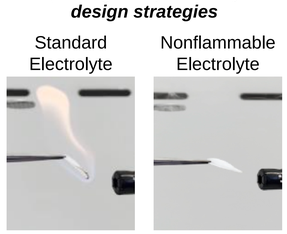

Newer work studies decomposition of nonflammable additives.

Ells, A.; May, R.; Marbella, L.; *ACS Appl. Mater. Interfaces.* **2021,** *13*, 53841; Ells, A.; Buitrago, P.; Marbella, L. *in preparation*

Evaluating the safety limits of Li-ion batteries

As the electrification of the global economy continues to accelerate, it is important to understand the safety limits of the materials we put into our devices. Common cathode materials such as layered materials (LCO, NMC), spinels (LMNO), or olivines (LFP) provide a source of oxygen during extended or high-voltage cycling that leads to flammable runaway reactions. By coupling a novel procedure to electrically short LIBs with isothermal microcalorimetry (ITMC) and accelerating rate calorimetry (ARC), we can start to quantify how much damage a battery can take before it reaches thermal runaway. Furthermore, by using these techniques, we can determine which cathode materials provide the highest level of safety.

Isothermal Calorimetry and Electrochemistry

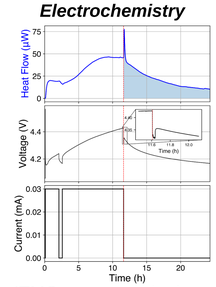

ITMC measures the heat evolution of a soft short

Experimental prototype cell

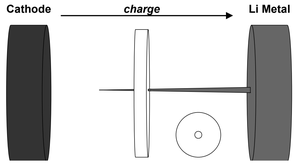

Experimental set-up to reproducibly grow filaments to induce shorting at the cathode.

SEM imaging

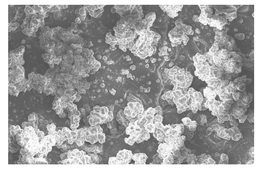

SEM confirms high surface area lithium filaments growing during charge

Accelerating Rate Calorimetry

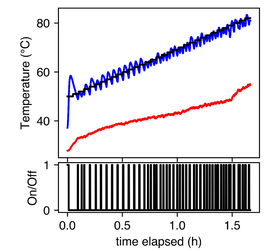

Homemade ARC measures thermal reduction

Probing interfacial reactivity of next-generation cathode materials

Li-, Ni- and Mn-rich layered transition metal oxides provide high energy densities while reducing cobalt dependence, making them promising candidates for next generation cathodes materials for Li-ion batteries. Unfortunately, these cathodes undergo structural rearrangement at high potentials that coincide with capacity fade and poor electrochemical kinetics. We use solid state nuclear magnetic resonance spectroscopy (SSNMR), solution NMR, and X-ray photoemission electron microscopy (XPEEM) to characterize interfacial degradation in these systems.

Solid-state NMR

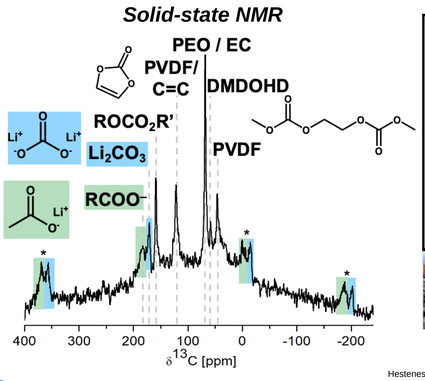

Solution NMR ***XPEEM***

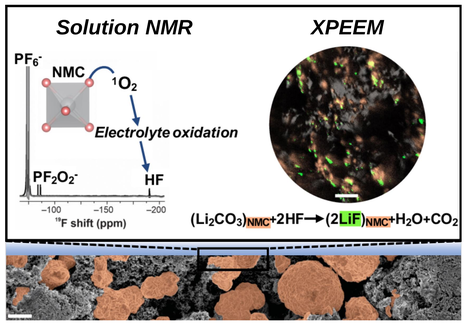

Mosaic model for CEI on NMC811

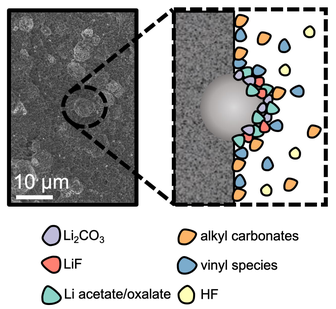

Hestenes, J. C.; May, R.; Sadowski, J.; Munich, N.; Marbella, L. E. *Chem. Mater.* **2022**, *34*, 232; Hestenes, J. C.; Ells, A. W.; Navarro Goldaraz, M.; Sergeyev, I.; Itin, B.; Marbella, L. E. *Front. Chem.* **2020**, *8*, 681.

Using electrolyte additives to control electrode surface stability

Control: **LP30 + Additive**

4% wt VC

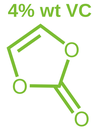

When electrolyte solutions decompose during a charge/discharge, electrolyte decomposition products either dissolve into solution or deposit onto electrode surfaces. Vinylene carbonate (VC) additive can suppress the rocksalt reconstruction on the surface of NMC811. X-ray photoelectron spectroscopy (XPS) show that VC increases the concentration of F-containing components and lowers the amount of O- and P-containing compounds, which may explain its surface-stabilizing effects in NMC811.

Capacity Retention

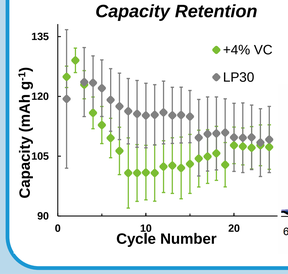

XPS F 1s of Cycled NMC811

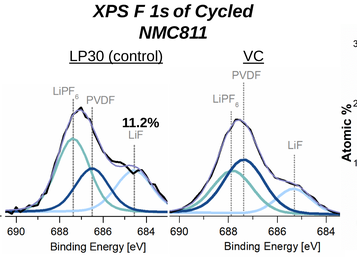

Composition of CEI

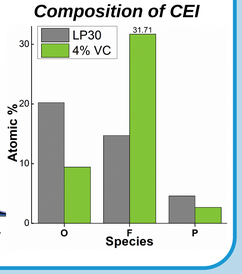

Acknowledgements

The Marbella Lab

Left to right: (top row) Drew, Eric, Bret, Lauren, Cameron, Lafe, Asya
(bottom row) Pablo, Emily, Naiara, Emily, Susie
Not pictured: Lakshmi

BNL CFN DOE DE-SC0012704
Botwinick-Wolfensohn Foundation DARPA EMBER

Research in the McNeill Group

V. Faye McNeill, Do Young Maeng*, Forwood Wiser†

Department of Chemical Engineering, Columbia University, New York, NY, USA 10027

vfm2103@columbia.edu +1 (212) 854-2869

COLUMBIA | ENGINEERING
The Fu Foundation School of Engineering and Applied Science

NATIONAL SCIENCE FOUNDATION · EPA · ALFRED P. SLOAN FOUNDATION · USAID FROM THE AMERICAN PEOPLE

Atmospheric Aerosol

- Condensed-phase particles suspended in a gas
- Diameters range from a few nm to tens of µm
  - EPA regulates particles below 10 µm in diameter[1]
- Human health, air quality, and climate effects due to ability to penetrate deep within lungs, scatter and absorb light, and act as cloud condensation nuclei (CCN)

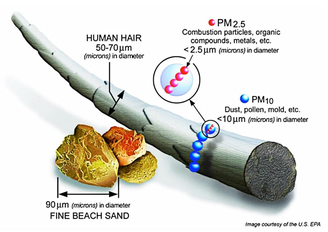

Secondary Organic Aerosol (SOA)

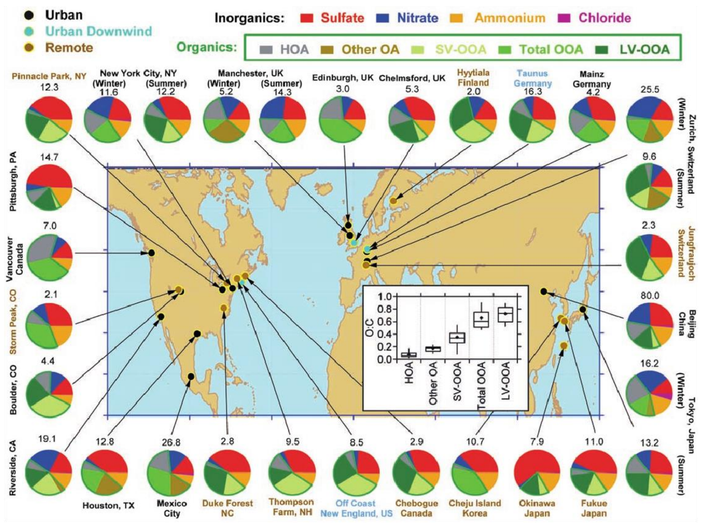

- Organic material is ubiquitous in atmospheric aerosols[2]
- Referred to as SOA when formed from precursor gases (known as volatile organic compounds or VOCs) in the atmosphere rather than being directly omitted
- Current models typically underestimate organic mass compared to observations

Aqueous Aerosol SOA (aaSOA)

- Water-soluble VOC uptake into aerosol water followed by particle-phase reactions yield low-volatility material
- Evidence from the field:
  - Correlation of water-soluble organic carbon (WSOC) with aerosol liquid water[3]
  - Oligomers, organosulfates
- Likely important in areas with high aerosol sulfate, humidity, and BVOCs (e.g. SE USA)

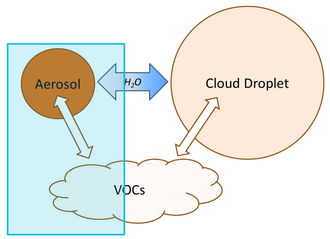

Gas-Aerosol Model for Mechanism Analysis (GAMMA)*

- Photochemical box model with coupled gas and aqueous aerosol chemistry
- Aqueous aerosol-phase SOA formation from gas-phase oxidation of isoprene, acetylene, toluene, xylenes
- Latest mechanisms of aqueous-phase brown carbon and organosulfate formation incorporated

McNeill et al., *ES&T* (2012)
Woo et al., *Faraday Discuss.* (2013)

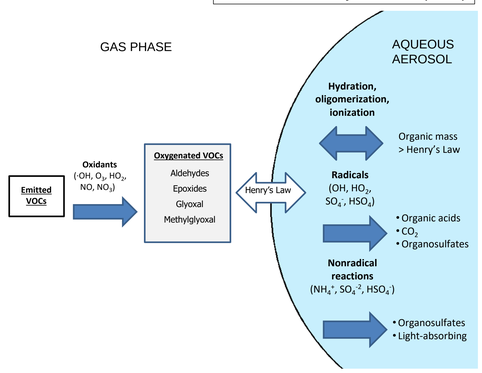

Atmospheric Chemistry Model Reduction (AMORE)†

- Using graph theory to simplify atmospheric chemical mechanisms
- Focusing on reducing isoprene mechanism of 400 species and 800 reactions down to less than 15 species and 20 reactions while retaining accuracy
- Isoprene is a major source of SOA and can contribute to tropospheric ozone
- Automated model reduction is key for accurate and timely modeling of atmospheric systems and accurately predicting SOA and other air quality metrics

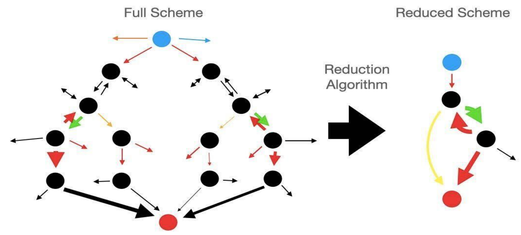

Clean Air Toolbox for Cities

- Adequate air quality monitoring networks are lacking for several cities with high levels of air pollution in India and Africa
- Closing the gap between data and knowledge, in collaboration with the people affected, is of utmost priority. This work entails:
  - Building up air pollution monitoring networks, data science and integration
  - Leading capacity building workshops, health effects analysis, exposure studies, and source identification

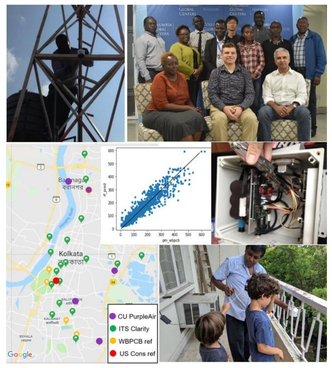

Chemistry of Indoor Environment*

- On average, Americans spend 87% of their time indoors.[1] However, indoor air chemistry has not been studied extensively.
- Man-made esters (MMEs) are abundant in indoor air,[4] as they are commonly used in consumer products and building materials.
- In damp environments, but they can hydrolyze on indoor surfaces and form products that negatively affect our health.
- To better assess and predict indoor air quality, we:
  - Investigated the kinetics of MME hydrolysis reactions via experimental studies[5]
  - Adapted GAMMA for indoor environments

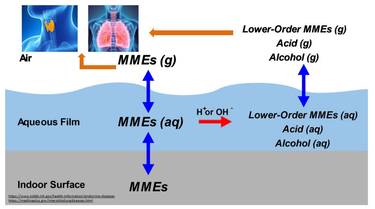

Room-Level Ventilation in Schools and Universities*

- Ventilation is of primary concern for maintaining healthy indoor air quality and reducing the spread of airborne infectious disease, including COVID-19
- For many universities and schools, however, ventilation data on a room-by-room basis are not available for classrooms and other key spaces.
- Ventilation measurements were conducted and reported along with the results from other ventilation studies performed in several different institutions in the U.S., highlighting the commonalities and differences in ventilation in buildings with varying ages, types, and locations[6]

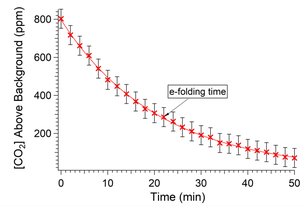

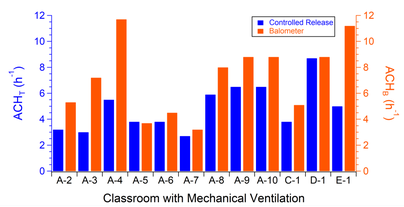

SOA Formation via Photosensitized Reactions

- Flow tube experiments[7,8] show particles containing humic acid grow in the presence of VOCs and UV light.
- We will perform chamber experiments in our new, custom-built photochemical reactor for varying, atmospherically relevant temperatures, relative humidities, and photosensitizer and VOC concentrations.

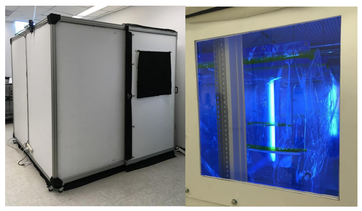

References

1. US Environmental Protection Agency
2. Jimenez et al., *Science*, 2009
3. Hennigan et al., *Atmos. Chem. Phys.*, 2009
4. Weschler et al., *Atmos. Environ.*, 2008
5. Maeng et al., *Int. J. Chem. Kinet.*, 2022
6. McNeill et al., *Atmos. Environ. X*, 2022
7. Monge et al., *Proc. Natl. Acad. Sci.*, 2012
8. Aregahegn et al., *Faraday Discuss.*, 2013

Hydrometallurgical Production of Domestic Metals for Energy Transition

West Group – Critical Materials

Contact: acw7@columbia.edu

COLUMBIA ELECTROCHEMICAL ENERGY CENTER

Introduction and Background

Increasing domestic mining and mineral processing capabilities is vital for national and economic security.

Permits for smelters are scarce
New technologies:
- Must be economical and scalable
- Minimize local environmental impacts
- Low or negative carbon footprint

Significant Cu-sulfide resources are available in the Americas. The Cu-concentrate is often shipped to smelters in Asia, for production and refining [Ling Zhang *et al*, *Science of The Total Environment*, **601–602**, 1238 (2017).]

Tamarack resource (Talon Metals, Operator)

- High-Mg rich ultramafic intrusive rocks are the primary minerals for carbonation
- Energy Relevant Metals

Total Indicated	8,504	1.13	0.92	0.03	0.34	0.21	0.17	8	2.54
Total Inferred	**8,461**	**0.83**	**0.55**	**0.02**	**0.23**	**0.13**	**0.13**	**3**	**1.19**

All resources are *in situ* and reported at a 0.50% Ni cut-off. Tonnage estimates are rounded down to the nearest 1,000 tonnes. Fe% in sulphides is based on a calculation of stoichiometric Fe concentration in Pentlandite and Pyrrhotite. NiEq grade based on metal prices of $9.50/lb Ni, $3.75/lb Cu, $25.00/lb Co, $1,000/oz Pt, $1,000/oz Pd and $1,400/oz Au using the following formula: NiEq% = Ni% + Cu% x $3.75/$9.50 + Co% x $25.00/$9.50 + PtEq/$31.103 x $1,000/$9.50/22.04 + PdEq/$31.103 x $1,000/$9.50/22.04 + AuEq/$31.103 x $1,400/$9.50/22.04. Fe is not included in the NiEq calculation. Mining recovery and dilution factors have not been applied to the estimates. No adjustments were made for recovery or payability

Talon's Proven Exploration Capabilities in a Short Timeframe

- 98% increase in the amount of contained nickel in the indicated

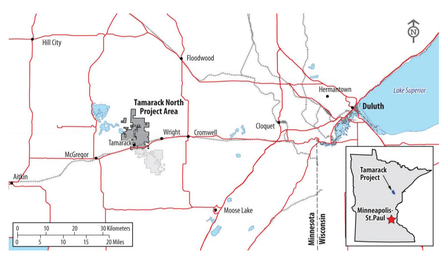

Preliminary Results

Past work has focused on RLEERT applied to Cu-sulfides exclusively
- Fast leach kinetics are necessary for economical processing
  - Target: <1hr Residence Time

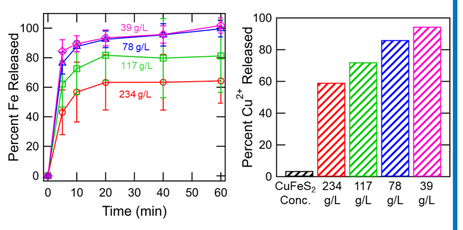

Multiple concentrates with varying mineralogy tested

Freeport: $CuFeS_2$ (Chalcopyrite) + FeS_2 (Pyrite)
Kennecott: $CuFeS_2$ (Chalcopyrite) + Secondary sulfides
Kamoa: Cu_5FeS_4 (Bornite) + Secondary sulfides
(Very low iron content)

Cu products identified depending on reagents used and operating conditions

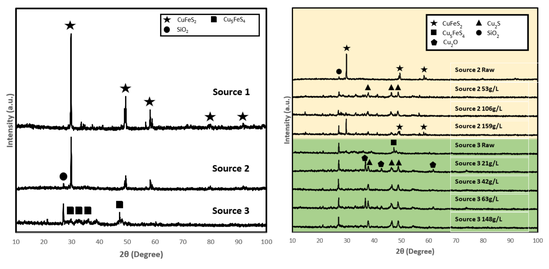

Continuous flow reactors have been demonstrated at 0.5-2.4 kg/day

OLEERT has also been proven to operate at room temperatures
- Safer -- Does not produce H_2S
  - Target: <1day Residence Time

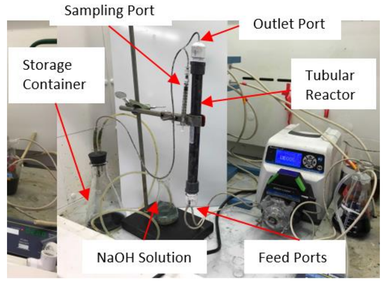

RLERRT and OLERRT: Reductive (or Oxidative) with Electrochemical Reagent Regeneration Technology

major energy-relevant minerals:
$CuFeS_2$, $(Ni,Fe)_9S_8$

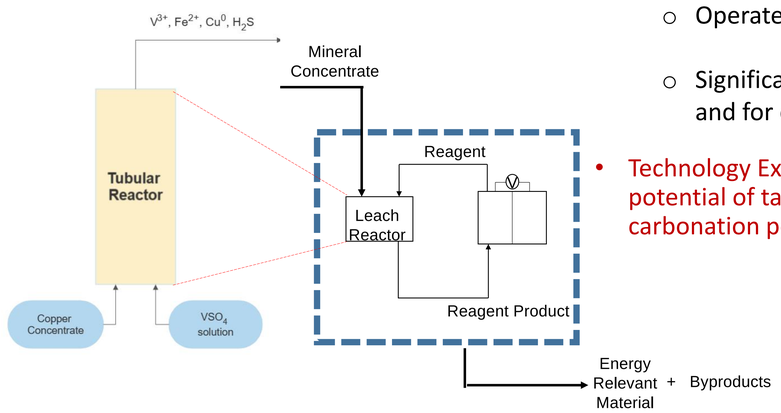

- Broad Vision: Replace Smelters with Redox Mediated Leaching
  - Operates at room temperature and pressure
  - Significant opportunities for improved yields and for domestic production
- Technology Extension: Reduce acid generating potential of tailings without impacting carbonation potential (Fe_7S_8)

Technology to Market

Customer Discovery

Detailed Techno-Economic Analysis (TEA)

- Existing TEA shows it is competitive with SOA for Cu
- Opportunities for off-spec Cu concentrate

Detailed Life-cycle Analysis (LCA)

- toward net zero Ni, Co and Cu
  - carbonation
  - powered by renewables
  - reduced comminution
- risk reduction of tailings

Handling of Valuable Elements and Penalty Elements

PGM, Au, Mo, Pb, Zn, Te, As …

Bringing it to Scale

STILLBRIGHT

Scale	Concentrate Feed Rate	Reactor Size
Bench (current)	2.4 kg/day	0.25 L
Continuous (current)	0.5 kg/day	~0.05 L
Bench (proposed)	24 kg/day	2.5 L
Pre-Pilot	1 MT/day	100 L
Pilot	10 MT/day	1 m^3
Commercial	100 MT/day	10 m^3

West Group

Understanding of Electrochemical Technologies and Systems which are Integral to Modern Life

arpa·e
U.S. DEPARTMENT OF ENERGY

O'SHAUGHNESSY GROUP

Neurotransmission in the Brain
SARS-CoV-2 Cell Entry

Synapses, Neurological Diseases
Antiviral Drugs to Block Infection

Modeling the Neurotransmitter Release Machinery

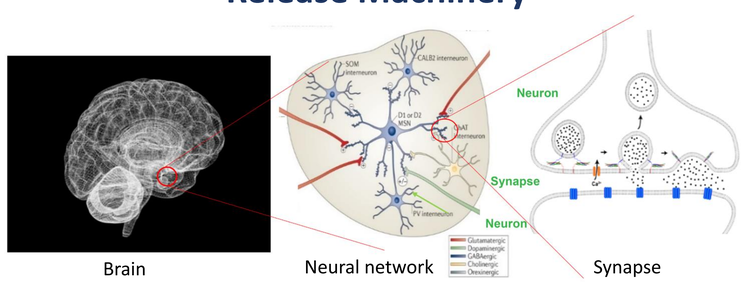

- Memory, cognition, sensation, coordinated motor activity
- Neurodegenerative & neurodevelopmental disorders

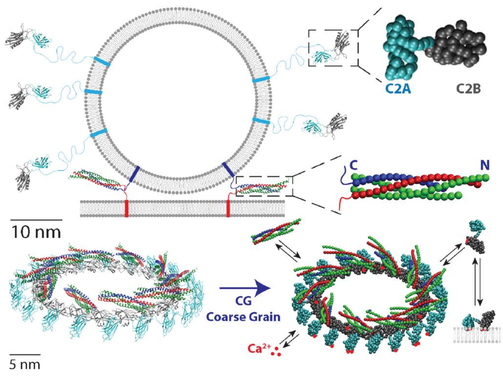

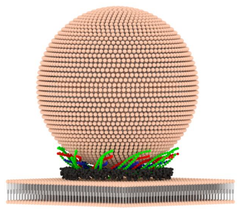

Molecular dynamics simulations reveal how this machinery senses Ca^{2+}, fuses the vesicular and neuronal membranes, and releases neurotransmitters.

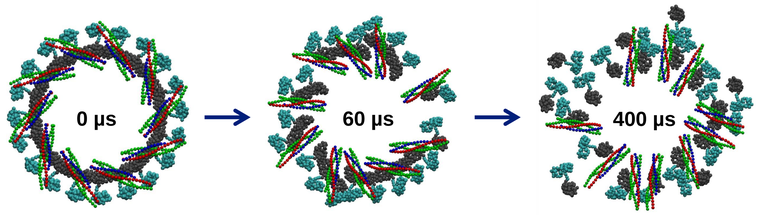

(1) Syt-mediated entropic force

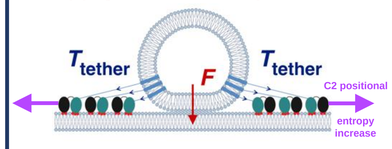

(2) SNARE-mediated entropic force

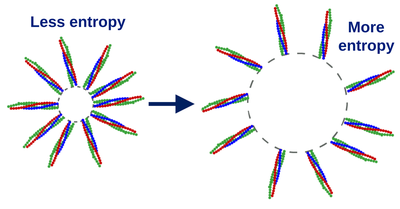

- 2 entropic forces drive fusion
  i. SNARE-mediated
  ii. Syt-mediated
- Increasing the number of SNAREs at the fusion site increases the magnitude of the entropic forces driving fusion, and accelerates the final fusion step

Core of the Fusion Machinery: SNARE Proteins

NON-ROD-SHAPED FUSOGENS

- Non-rodlike membrane-bound fusogens produced transient hemifusion and no fusion.

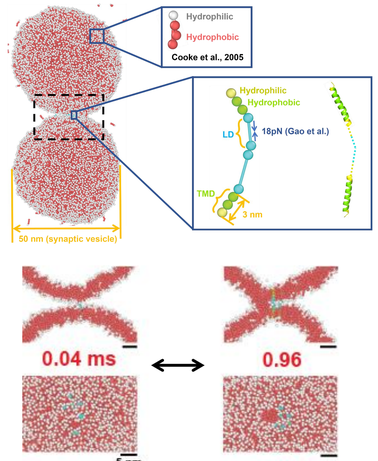

SNARE FUSOGENS

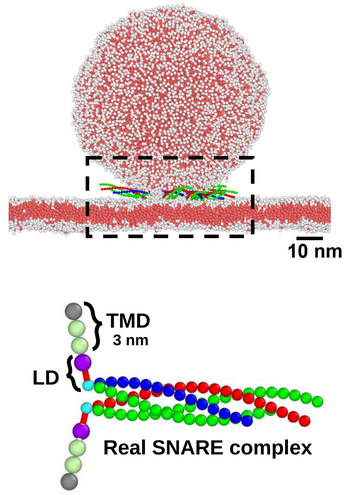

- Rod-shaped SNARE complexes are required to generate entropic forces to drive membrane fusion.
- Entropic forces push SNARE complexes away from the contact zone within a microsecond, allowing membrane contact.

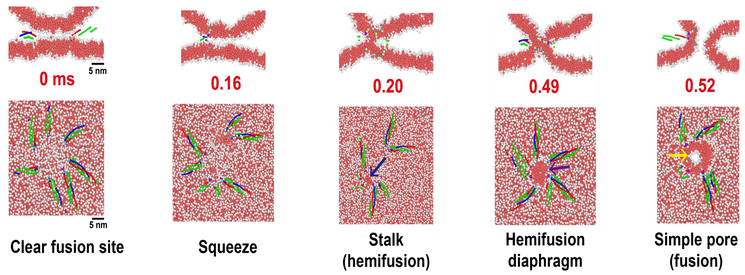

- More SNAREs facilitated both hemifusion and fusion by providing higher entropic forces to press two membranes together.

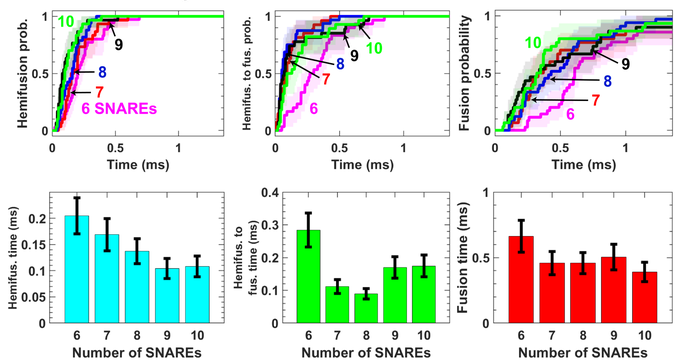

Cell Entry by the SARS-CoV-2 Virus

SPIKE PROTEIN

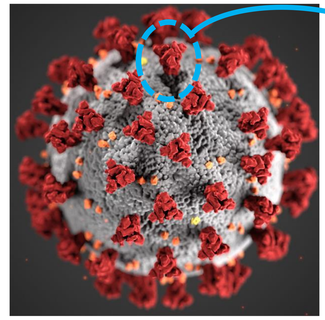

Extended Spike protein

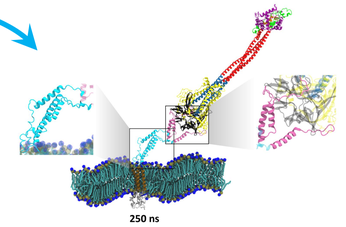

First ever atomistic simulations of the extended unraveled Spike protein that captures and enters cells

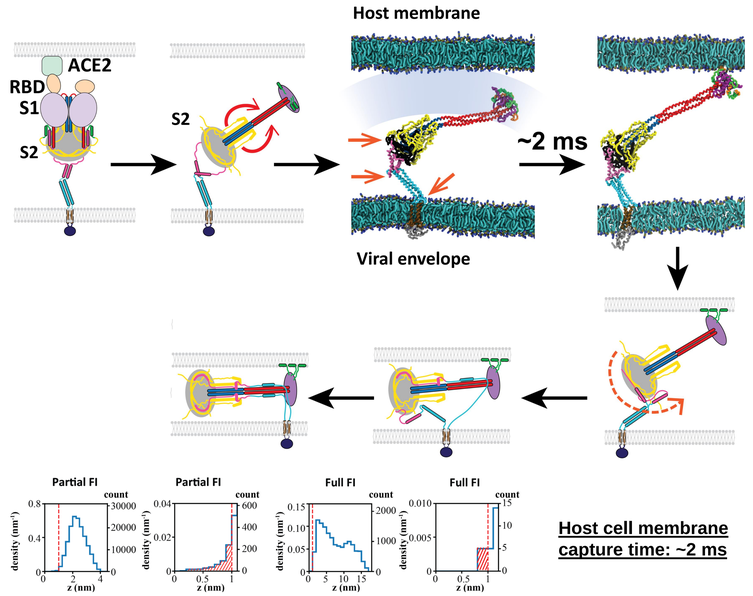

Host cell membrane capture time: ~2 ms

- Infection pathway: extended spike protein captures target cell, refolds and enters cell
- Modeling pathway, mechanisms
- Discovering novel drugs that blocks cell entry

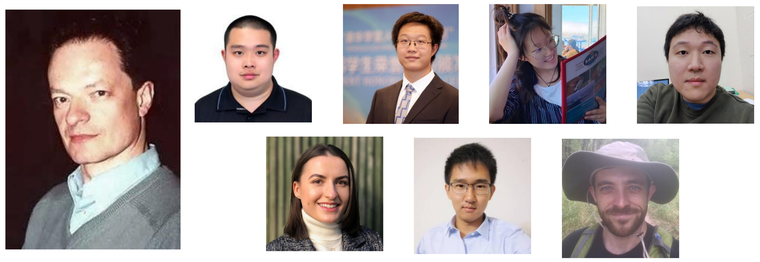

Building Deep Learning Models to Understand Important Biological Questions

O'Shaughnessy Group

Department of Chemical Engineering, Columbia University, New York, NY

SNARE-mediated Membrane Fusion

- SNARE proteins constitute the core of the cellular membrane fusion machinery.

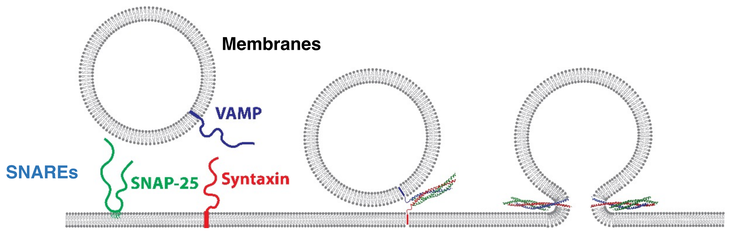

- Coarse-graining SNAREpins: VAMP complexed with Syntaxin and SNAP-25.

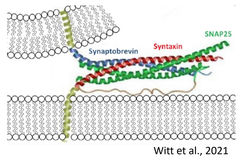

Witt et al., 2021

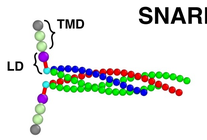

- Experimental fusion timescale (ms to s) is beyond the reach of atomistic simulations or widely used coarse-grained (CG) forcefields, e.g. MARTINI.

- Our ultra coarse-grained vesicle-vesicle fusion system with SNAREs:

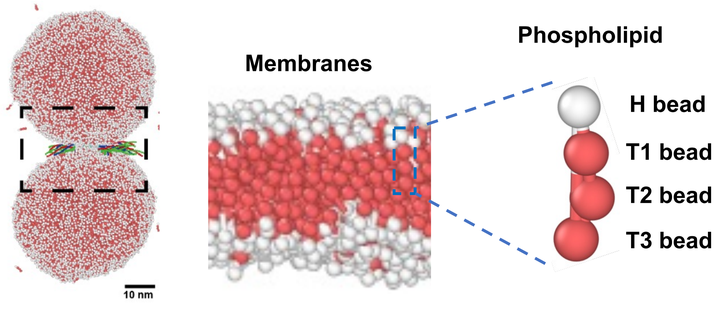

- Simulating tens of thousands of phospholipids and a multiprotein machinery for milliseconds is highly computationally demanding.

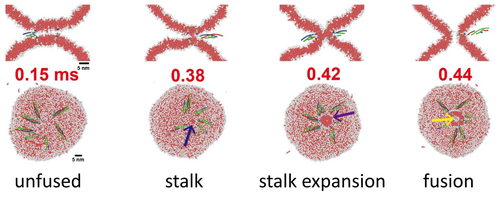

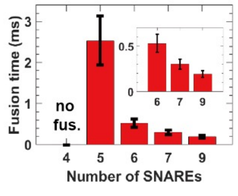

- Deep learning models can recognize patterns in complex systems.
- Can we identify a pathway for membrane fusion?

Neural Network to Extract Collective Variables

- We trained the model using a training set including ~ 29k states from 5 independent simulations.
  - Unfused states: ~ 11k
  - Stalk states: ~ 8k
  - Fusion states: ~ 10k
- The model successfully classified the test set (10k states from 5 extra simulations) with > 99% accuracy.
- Based on this model, we extracted the collective variables of the SNARE-mediated membrane fusion process

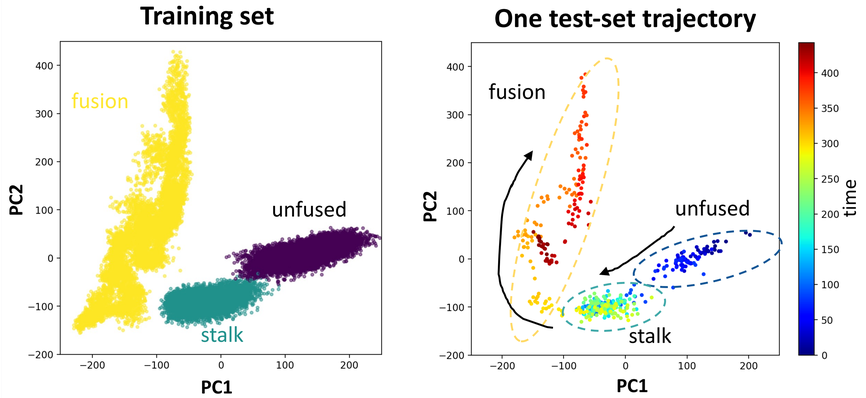

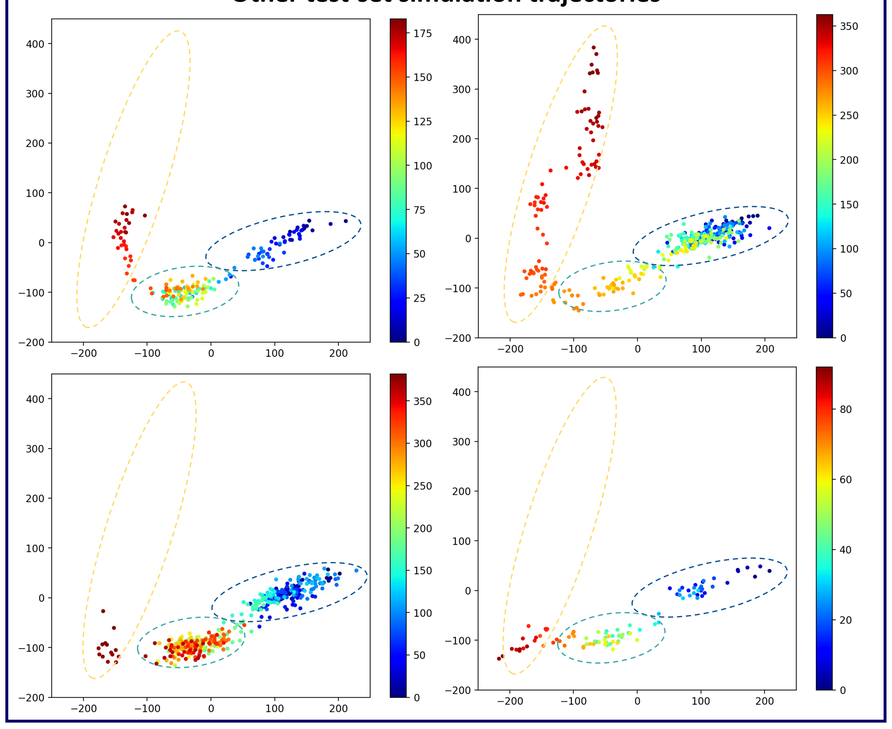

The Membrane Fusion Pathway

- We extracted a pseudotime τ that describes the membrane fusion pathway.

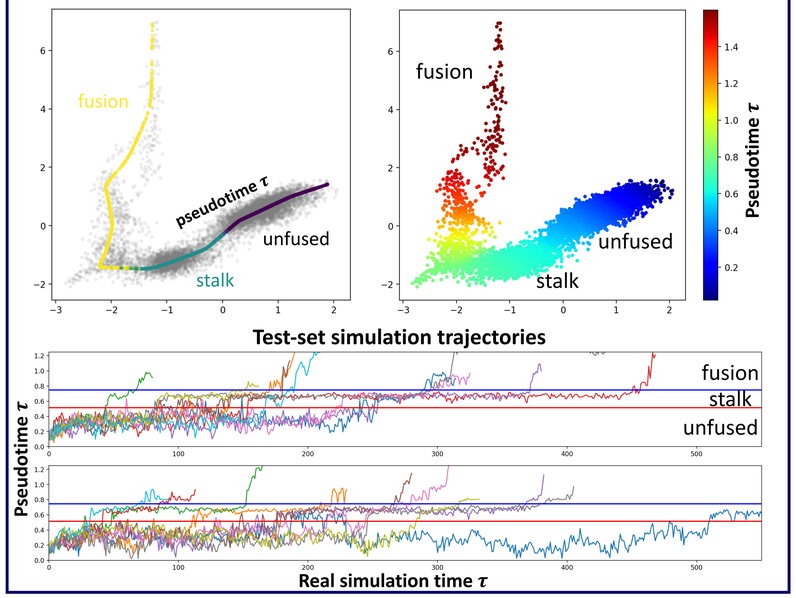

Understanding the glassy cytoplasm

- We built a neural network model to classify the trajectories of anomalous diffusive particles (i.e., tracer particles in the glassy cytoplasm) into Continuous-Time Random Walk (CRTW), Fractional Brownian Motion (FBM) and Lévy Walk (LW), and achieved high accuracy.

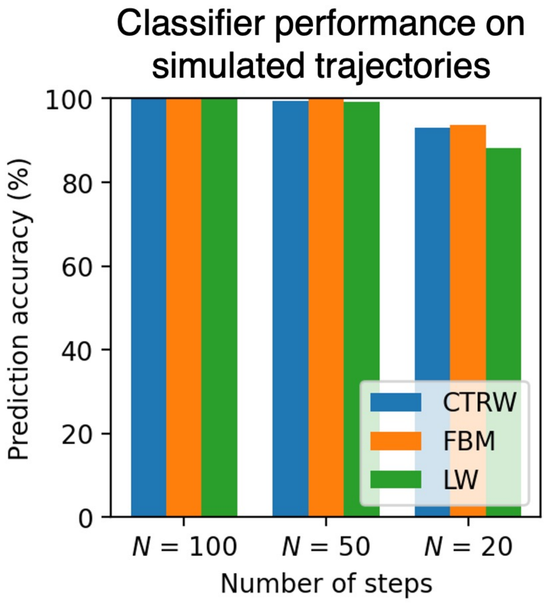

Using Computational Methods to Investigate Morphogenesis during Embryo Development

O'Shaughnessy Group

Department of Chemical Engineering, Columbia University, New York, NY

Drosophila Ventral Furrow Formation

First morphogenesis event during *Drosophila* embryo development
Ventral furrow formation during *Drosophila* (fruit fly) gastrulation requires tissue contraction and folding.

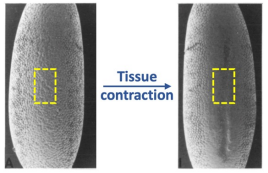

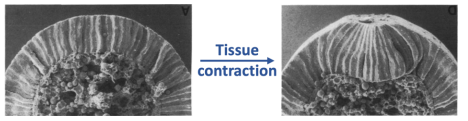

(Sweeton et al., 1991)

MODEL

- **The tissue folding is driven by myosin, whose supracellular profile has a bell-shaped envelope.**

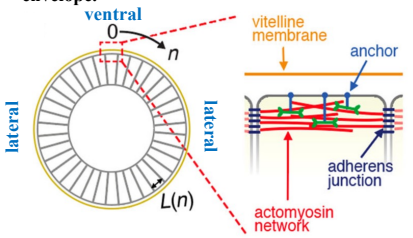

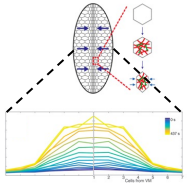

(Heer et al., 2017)

Force Balance On Each Cell

Force due to actomyosin tension + Internal viscous force + External drag force = 0

Characteristic length scale $\xi \approx 2.5$ cells.

RESULTS

- **Myosin Curvature Drives Tissue Folding**

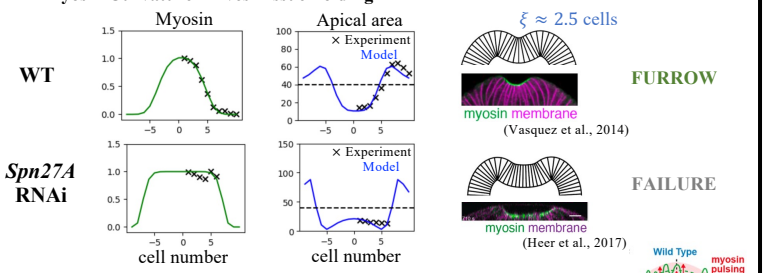

(Vasquez et al., 2014)

(Heer et al., 2017)

- **Myosin Pulsing Rescues Tissue Folding from Unavoidable Fluctuations**

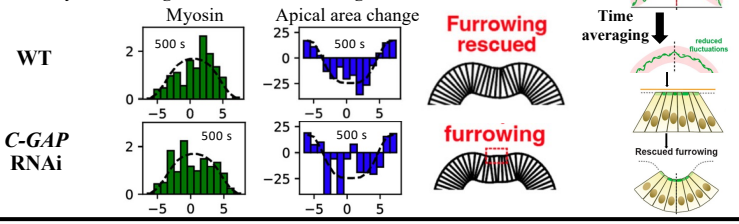

Drosophila Germ-band Extension

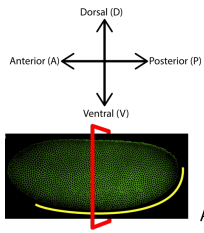

Fernandez-Gonzalez et al., 2009

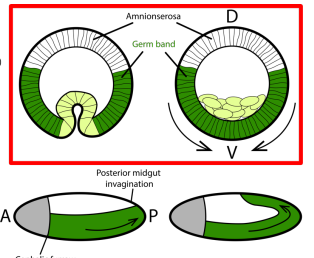

Right after ventral furrow formation *Drosophila* germ band undergoes convergent extension and doubles its length in the AP direction and narrows in the DV direction.

MODEL

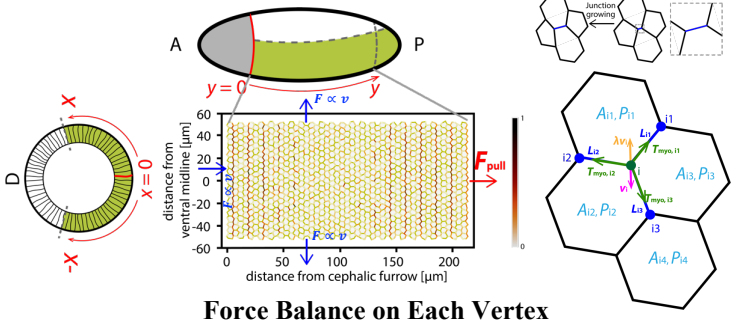

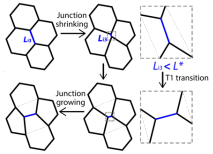

Force Balance on Each Vertex

Actomyosin contractile forces + Internal viscous forces + Restoring elastic forces + External drag forces = 0

RESULTS

- **Germ-band extension requires both myosin cables and posterior pulling forces.**

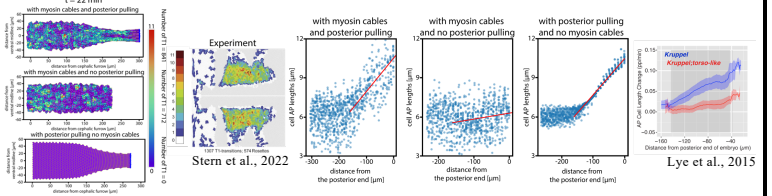

Stern et al., 2022

Lye et al., 2015

- **Dilute myosin cables are required for cell intercalation and rearrangement**

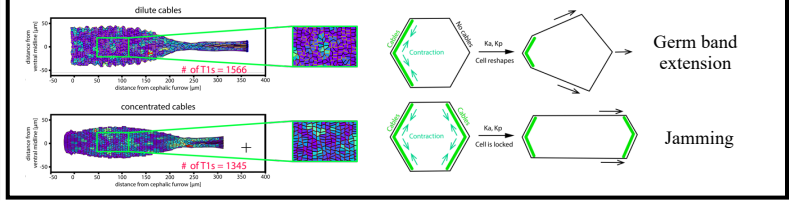

Cell Apical Constriction Driven by Actomyosin Networks

- **Tissue contraction and folding during *Drosophila* (fruit fly) gastrulation is driven by apical actomyosin networks in individual**

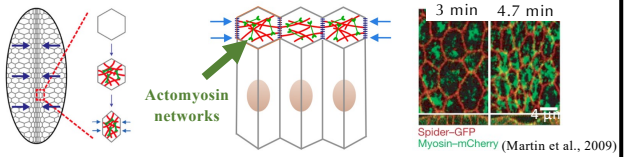

(Martin et al., 2009)

Molecularly Explicit Simulation

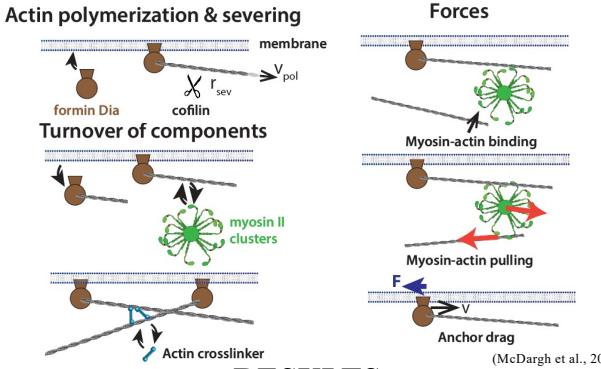

(McDargh et al., 2021)

RESULTS

- **Apical Networks Spontaneously Form**

Experiment

Drosophila posterior midgut invagination
Myosin membrane

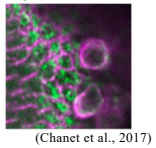

(Chanet et al., 2017)

Simulations

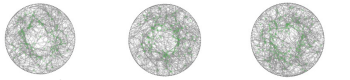

Simulated fluorescence microscopic images (myosin)

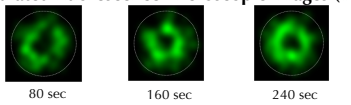

- **Network Morphology Depends on Filament Lengths**

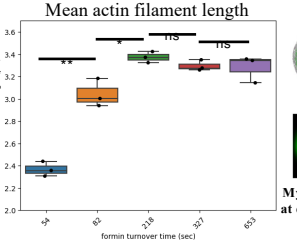

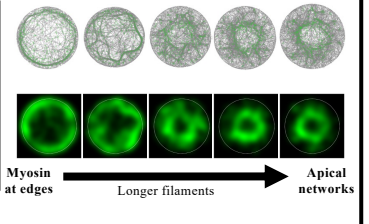

KUMAR GROUP

SOFT MATERIALS FOR SUSTAINABILITY

Machine Learning

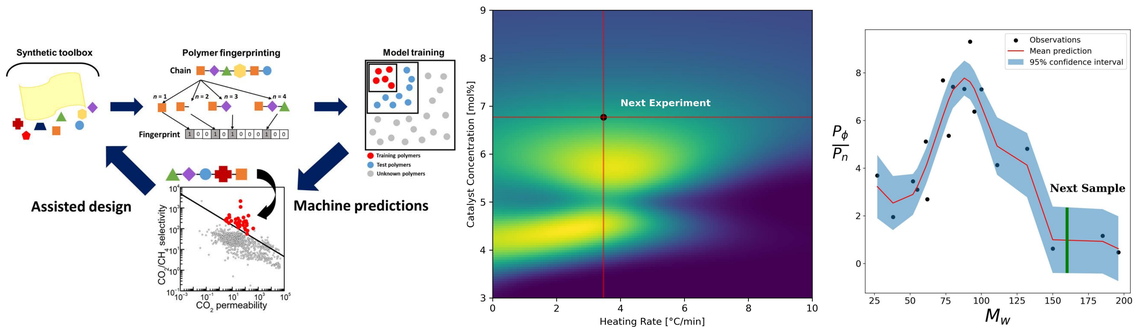

Upcycling

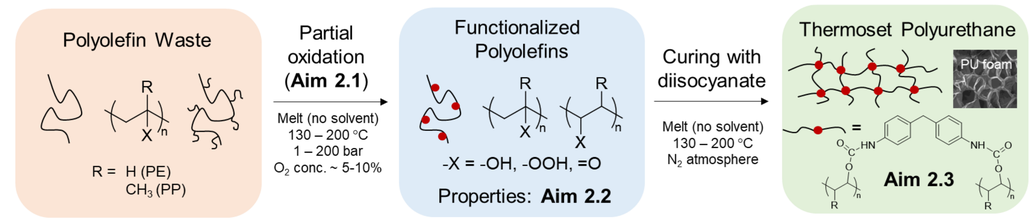

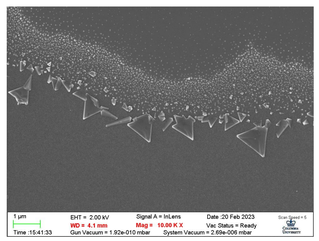

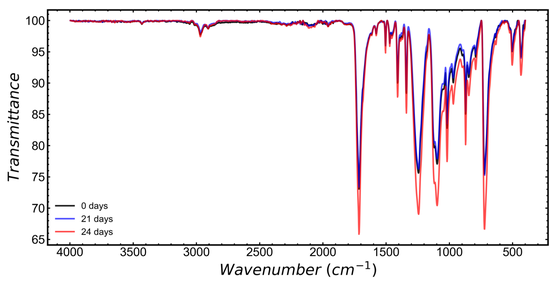

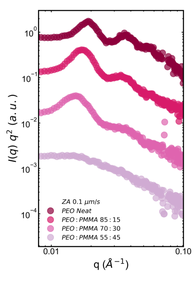

Tuning Nanoparticle Dispersion

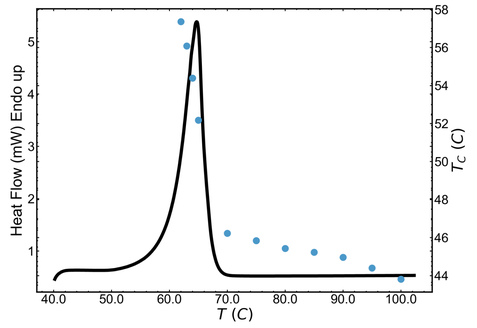

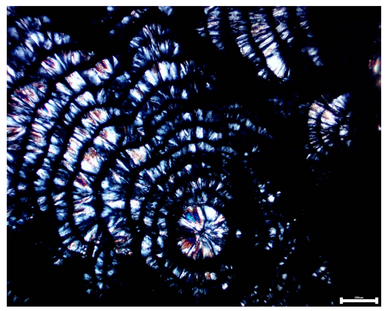

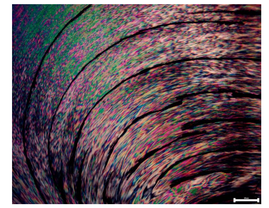

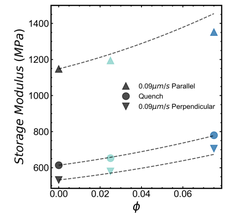

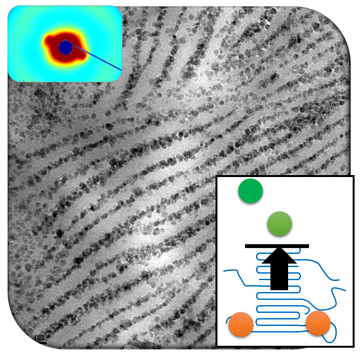

Polymer Crystallization

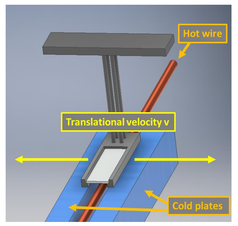

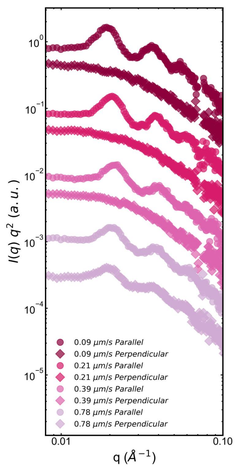

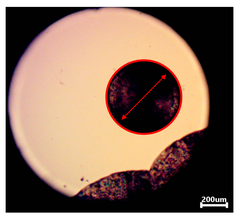

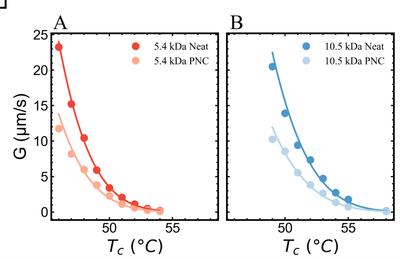

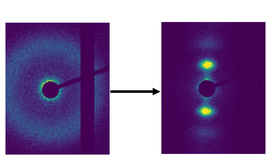

Ion Transport in Soft Nanomaterials

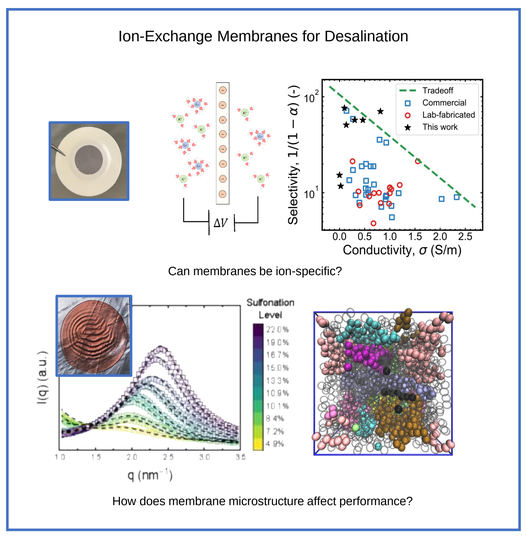

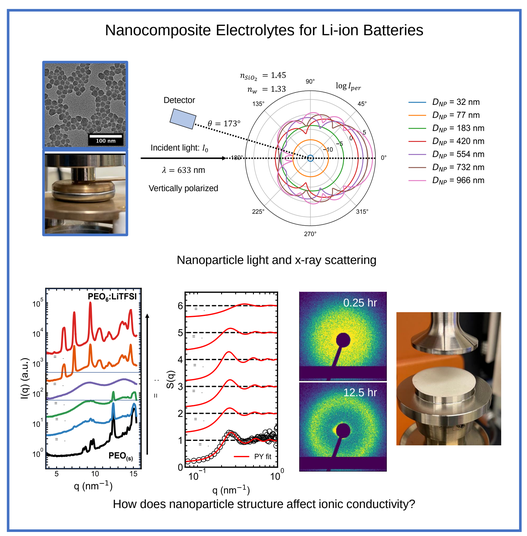

Nanocomposite Gas Separation Membranes

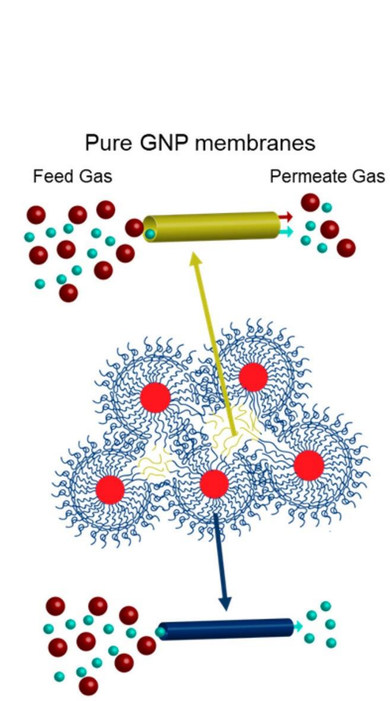

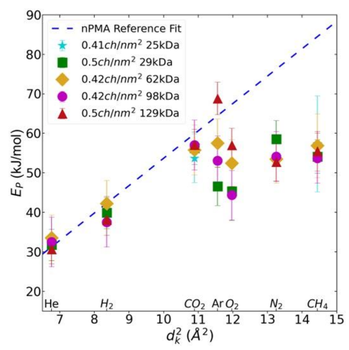

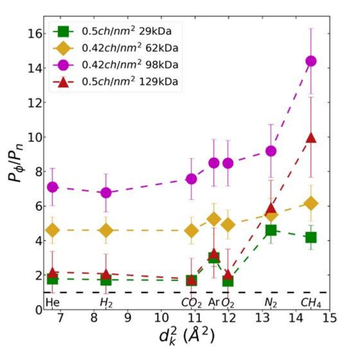

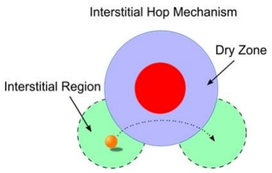

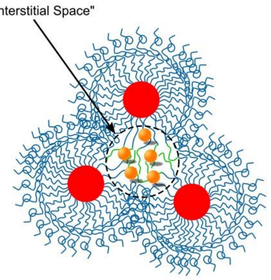

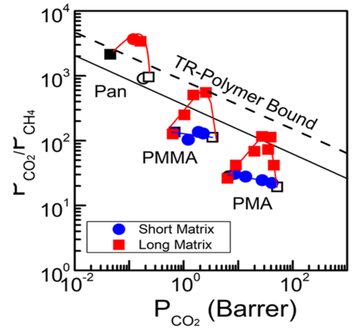

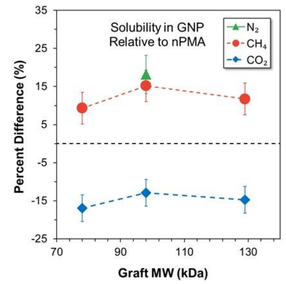

Extraction and Recovery of Critical Elements from Waste-to-Energy Ashes using CO_2 via Carbonation and Ligand Design

Amanda Whai Shin Ooi, Hunter B. Vibbert, Seokyoon Moon and Ah-Hyung Alissa Park
Department of Chemical Engineering, Department of Earth and Environmental Engineering,
Lenfest Center for Sustainable Energy, The Earth Institute, Columbia University in the City of New York, New York, NY

Background and Objectives

Designing a sustainable process for the extraction and recovery of critical elements from unconventional resources for future manufacturing

- How do we extract metals from complicated and variable matrix at high purity?
- How does the presence of **competing metal ions (e.g., Ca, Na, K, Al, Fe)** and anions (e.g., Cl, S, P) affect the leaching and separation of targeted metals from wastes?
- What are key design parameters of **ligands** that can **selectively bind** to targeted metals including REEs and enhance downstream separation efficiency?

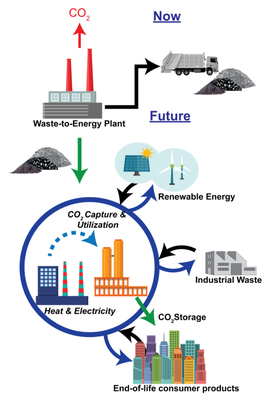

Using CO_2 in the hydrometallurgical extraction of WTE ashes

Characterization of heterogenous WTE ash

For 1 ton of municipal solid waste (MSW):
- 500 to 650 kWh of power
- About 50 lbs. of recycled metal
- **Ash: about 10% of original volume**

Fly ash containing volatile elements (e.g. Ca, Na, Zn etc.)

Composition	Wt. %
Ca	**26.7 (1)**
Si	2.7 (0.3)
Na	2.40 (0.7)
K	1.53 (0.3)
Al	1.40 (0.2)
Zn	**1.24 (0.3)**
Fe	0.80 (0.1)
Mg	0.80 (0.1)

SEM images and EDX mapping of major elements in fly ash sample

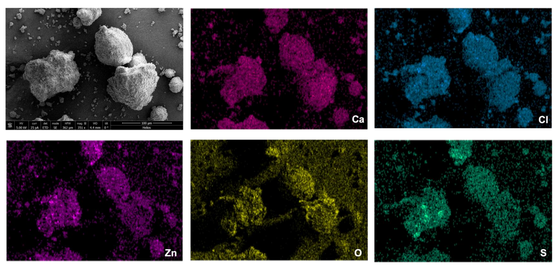

- Heterogenous distribution of elements in fly ash particles
- Need to convert them into usable forms

Comparison between using HNO_3 and CO_2 as leaching agents

Shrinking Core Model

$$1 - (1 - X)^{\frac{1}{3}} = kt$$

$$1 - 3(1 - X)^{\frac{2}{3}} + 2(1 - X) = kt$$

$$\frac{1}{3}\ln(1 - X) + (1 - X)^{\frac{1}{3}} - 1 = kt$$

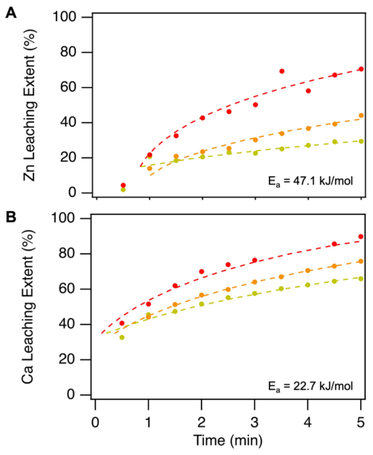

Comparison of dissolution extents of Ca and Zn using HNO_3 at pH 3, pH 6, and CO2 at pH 6 as a sustainable alternative acid source

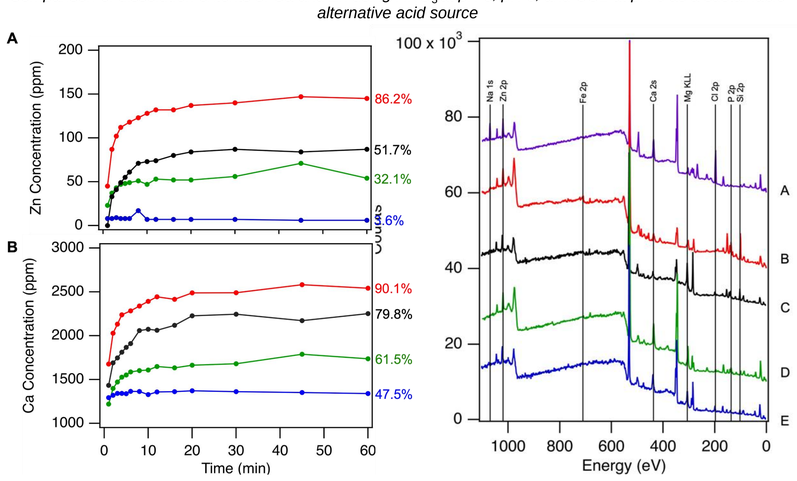

- Mg and Si show similar extraction kinetics when both leaching solvents are used
- HNO_3 was able to leach out significantly more Ca and Zn than CO_2 – precipitation of metals as silicates or aluminosilicates

Ca and Zn at limited by diffusion!

Comparison of metal extraction in four leaching pathways

Schematic of 4 different leaching pathways for fly ash, carried out at pH 3 and RTP conditions

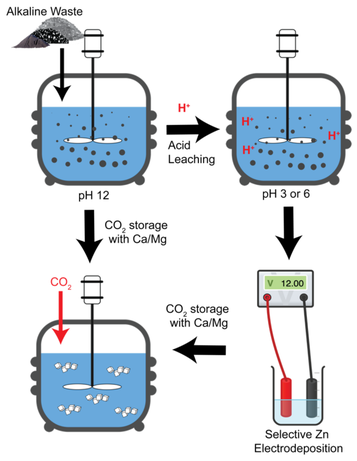

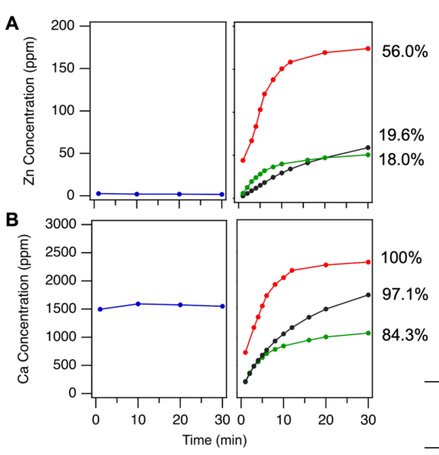

DI water washing stage selectively leaches Ca (and Na, K) into liquid phase, leaving all other elements in solid phase

- *At pH 3 conditions, extraction extent of Ca using CO_2 is higher compared to using HNO_3*
- *Extraction extent of Zn is similar after DI water wash stage*

	Single step acid leaching	Sequential leaching
pH 3 HNO_3	0.0434	0.0749
pH 6 HNO_3	0.0208	0.0387
pH 6 CO_2	0.0247	0.0472

DI water wash does not alter the extraction extents of Ca and Zn, but alters distribution of elements in leachate for downstream recovery

Recovery of Ce from leached ashes

Pathway for recovery of cerium using solvent extraction

Leachate via Hydrometallurgical Extraction contains high concentration of competing ions: Ca^{2+}, Mg^{2+}, etc..

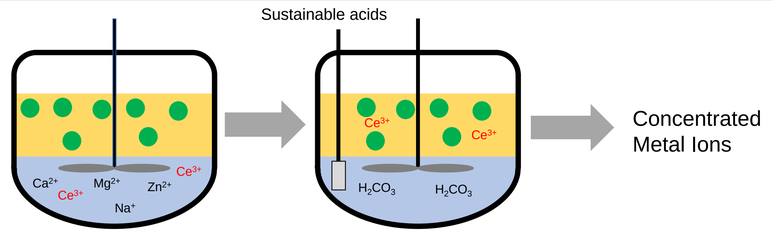

How can we develop an effective separation technology in the presence of competing ions?

Ligand Design for Mild Extraction and Regeneration Processes

Use of tripodal scaffold with modular functionality to selectively target Ce

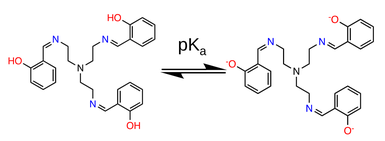

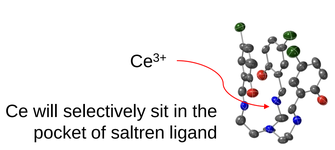

Ce will selectively sit in the pocket of saltren ligand

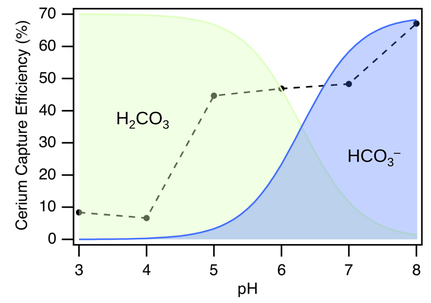

Trend of Ce recovery at different pHs imply that the protonation state of the ligand has a large impact on its binding with Ce

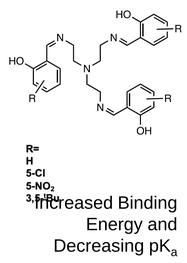

Increased Binding Energy and Decreasing pK_a

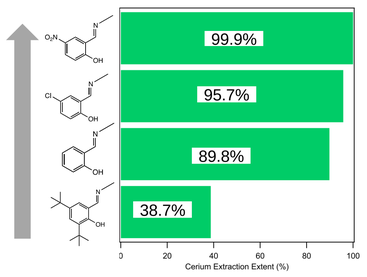

Relative steric bulk plots of saltren and saltren-tbut (75.9% v vs 81.4% v buried) ligands from DFT calculations

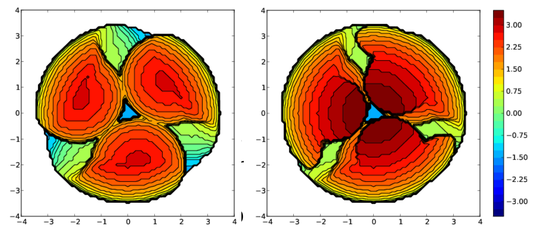

Using strong acids vs. milder CO_2 as protonation sources for ligand regeneration

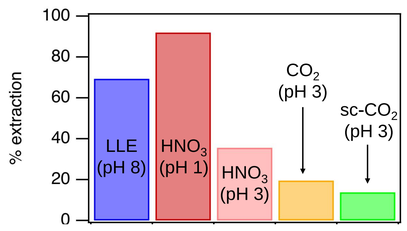

CO_2 Equilibrium

$$CO_2(aq) + H_2O \rightleftharpoons H_2CO_3(aq) \quad K_H$$

$$H_2CO_3(aq) \rightleftharpoons H^+ + HCO_3^-(aq) \quad K_1$$

$$HCO_3^-(aq) \rightleftharpoons H^+ + CO_3^{2-}(aq) \quad K_2$$

Potential Ce complex structures form during LLE process

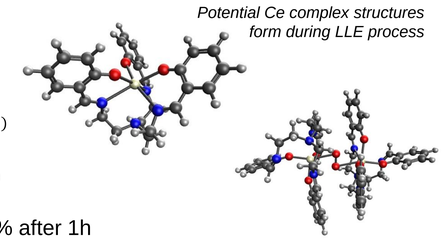

Re-extraction using CO_2 : 20% after 1h

Carbon mineralization to form high purity calcite

Recovery of Ca as calcite at pH 9 conditions

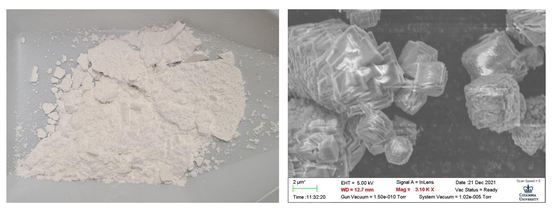

High purity calcite produced from carbonation of DI wash leachate (0.28 g calcite / g fly ash)

Elements	Composition (%)
Al	0.026
Ca	43.466
Fe	0.019
Mg	0.021
Si	0.080
Zn	0.066

Elements	Composition (%)
C	11.61
N	0
H	0
O	33.44

Can be used in the concrete, paint and coating industries

Future Directions

Scaffold used for Ce recovery are found in polymer canopy of poly(ethyleneimine), which is used in the Park group as a medium for CO_2 capture

Can we get the benefits of a hybrid material with non-thermal energy regeneration or separation **without** liquid-liquid extraction?

How does the binding properties and selectivity change when the small molecule ligand system is transferred to a hybrid system?

Schematic of selective recovery of Cu from leachate

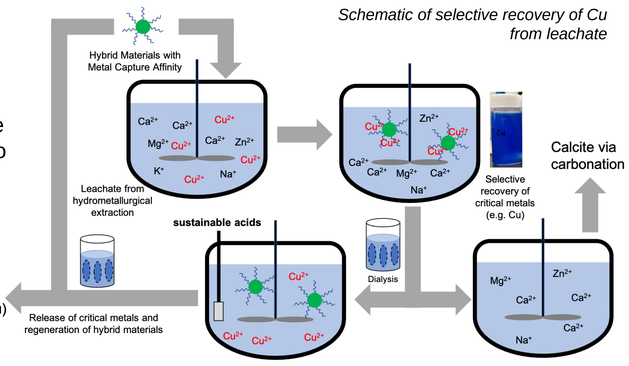

Acknowledgements

Collaborators: Prof. Xiao Su at University of Illinois Urbana-Champaign

Financial support: DOE ARPA-E and Lenfest Center for Sustainable Energy, Earth Institute, Columbia University

Gang Group: Architecture and Animation of Nanoscale Matter

Designed Self-Assembled Nanomaterials

Objectives

Nano-components + Desired organization

Functional nanomaterials

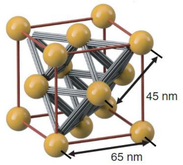

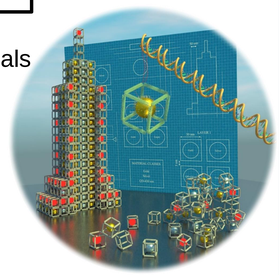

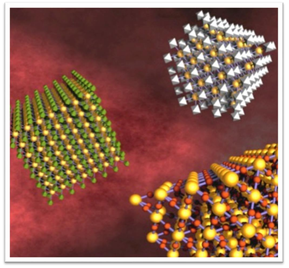

Novel self-assembly methods:
- Optical components
- Chemical properties
- Enhanced sensing
- Mechanical attributes
- Improved catalysis

Y. Zhang et al., Nature Nanotechnology, 8 (11), 865 (2013)
J. Kahn, O. Gang, Angewandte Chemie, 134 (3), e202105678 (2022)
A. Michelson et al., Science, 376 (6589), 203-207 (2022)

DNA Assembly

Particle cores are inorganic, carry function.

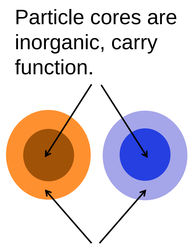

Shells from DNA dictate interactions.

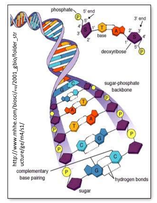

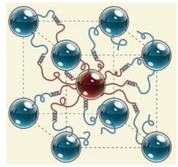

D. Nykypanchuk et al, Nature, 451, 549 (2008);
H. Xiong et al, 130, 8, 2442–2443 JACS (2008)

From Clusters to Lattices through Shape Coordination:

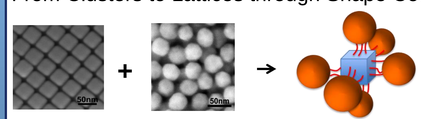

- Nano-cubes can direct spheres into formation of clusters with 6-fold coordination.

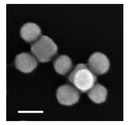

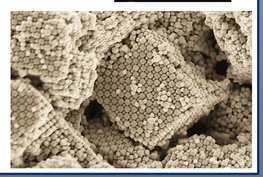

F. Lu, et al, Nature Comm., 6, 6912 (2015)
F. Lu, et al, Science Adv., 5, 5 (2019)

Prescribed 3D Structures

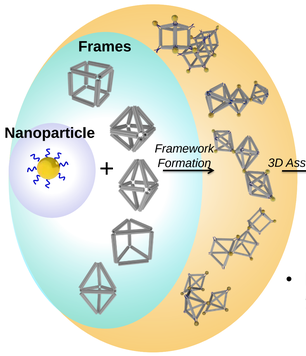

NP-DNA Framework

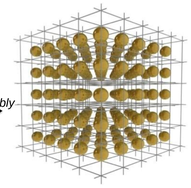

- DNA origami frames are used to coordinate nanoparticles.

Octahedron

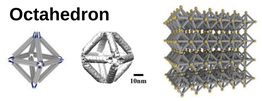

ESB

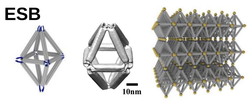

Cube

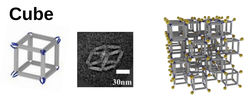

Prism

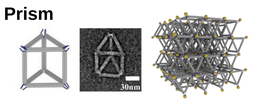

Y. Tian et al. Nature Materials 15, 654 (2016)
W. Liu et al. Science, 351, 582 (2016)

Bottom-up Nanofabrication Platform

3D Assembly via Valence-prescribed Material Pixels

Establishing a broadly applicable self-assembly platform

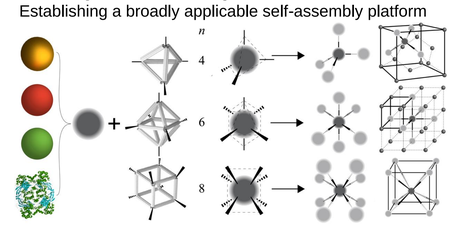

Self-Assembly by meso-voxels using "Colored" Bonds

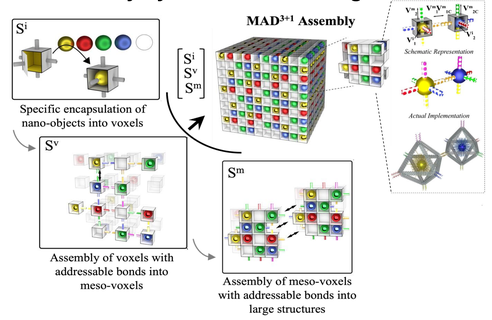

Y. Tian et al. Nature Materials, 19, 789–796 (2020); J. Kahn et al. ChemRxiv, 10. 26434 *(2022)*

How do we enable new functions with self-assembled nanomaterials?

3D Nanoreactors

Enzyme Arrays for Catalytic Cascades

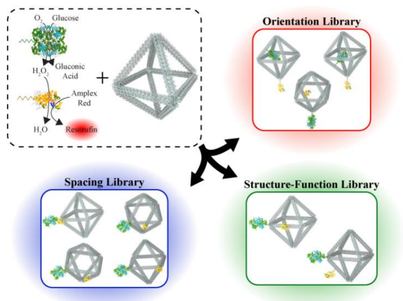

Nanoscale arrays of 3D DNA origami can be programmed to arrange enzymatic cascades to study the relationship of their nanoscale organization and their activity.

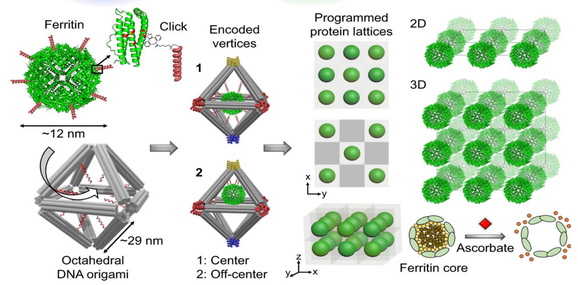

J. Kahn, et al. JACS Au 2, 2, 357–366 (2022)
ST, Wang et al., Nature Comm. 12, 3702 (2021)

Optical and Electronic Devices

Assembly of 3D Arrays of Quantum Dots

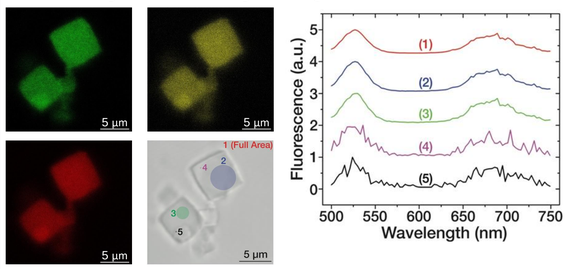

Y. Tian et al. Nature Materials, 19, 789–796 (2020)

3D Reconstruction of plasmonic lattices

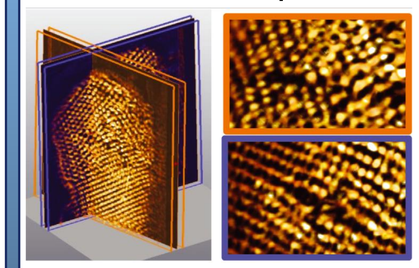

Nondestructive 3D imaging of complexly organized nanoparticles and multimaterial DNA frameworks

A. Michelson et al., Science, 376 (6589), 203-207 (2022)

Active Nano-Construction

Acoustic Organization of DNA lattice

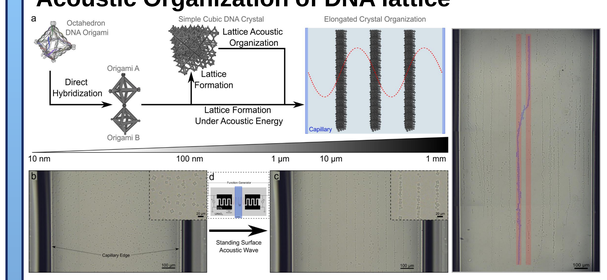

Acoustic waves arrange crystals into elongated structures at the millimetric scale

Dynamic DNA frames for 3D Nanoparticle Lattices

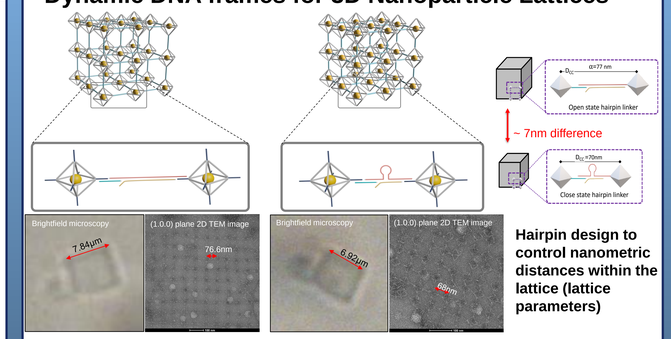

Hairpin design to control nanometric distances within the lattice (lattice parameters)

Recent Cover Features of the Gang Group

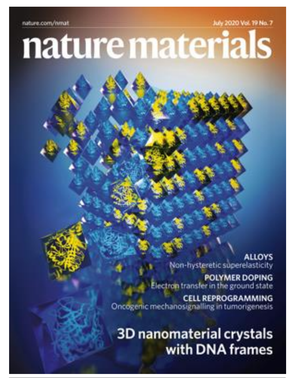

Acknowledgements: Research carried out at the Center for Functional Nanomaterials (CFN), National Synchrotron Light Source I & II (NSLS and NSLS II) was supported by the U.S. Department of Energy, Office of Basic Energy Sciences, under Contract No. DE-SC0012704, Department of Defense and National Science Foundation

Brookhaven National Laboratory
U.S. Department of Energy
Office of Science
DOD MURI
NSF
W.M. KECK FOUNDATION

Contact: oleg.gang@columbia.edu

COLUMBIA | ENGINEERING
The Fu Foundation School of Engineering and Applied Science

COLUMBIA ELECTROCHEMICAL ENERGY CENTER

COLUMBIA | ENGINEERING
The Fu Foundation School of Engineering and Applied Science

Research in the Urban Group

Understanding and Discovery of Materials for Clean Energy Applications

(Contact: au2229@columbia.edu)

Mission Statement

Computational Understanding and Discovery of Materials for Clean Energy Applications

Employ computational techniques to

- Understand phenomena in real-world materials that are hard to access experimentally
- Evaluate hypothetical materials before synthesis attempts for **accelerated materials discovery**

Research Program

Materials Interfaces in Electrochemical Energy Storage and Conversion

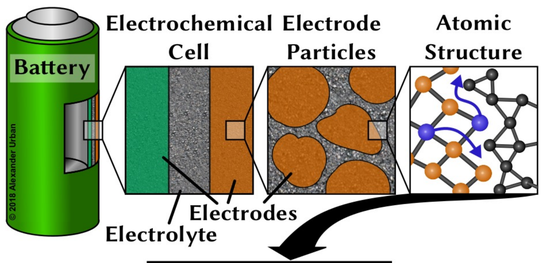

Transport Mechanisms → Rate Capability
Phase Diagrams → Voltage; Stability
Interfacial Reactions → Degradation Pathways

Interfaces in Batteries and Fuel Cells

Atomistic Simulations

Insight & Model

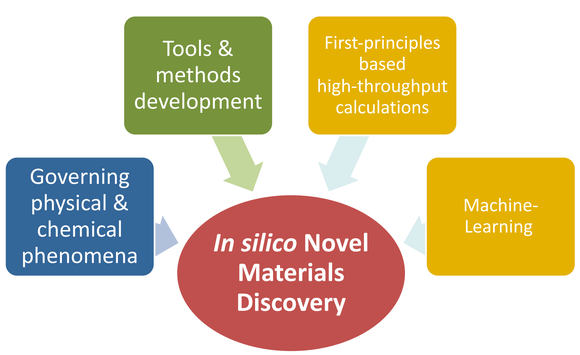

Machine Learning Augmentation

Example Project: Predicting high-temperature reaction chemistry

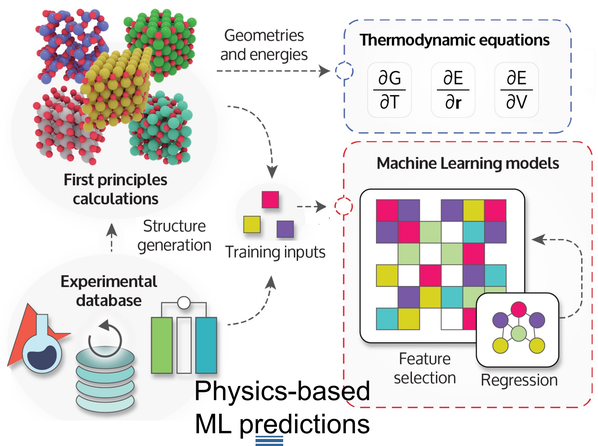

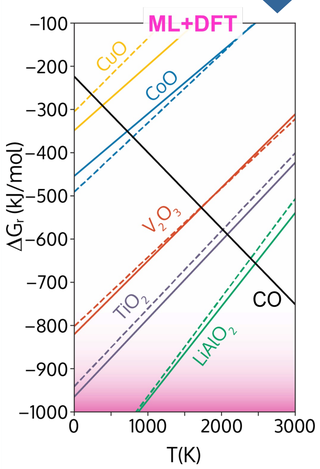

- Prediction of oxide reduction temperatures
- Zero kelvin from quantum mechanics + ML for temperature

Garrido Torres, Gharakhanyan, Artrith, Eegholm, Urban, *Nat. Commun.* **12** (2021) 7012.

Example Project: Representation Learning

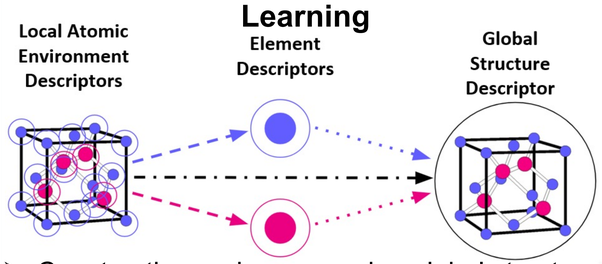

- Constructing and compressing global structure descriptors from local environments

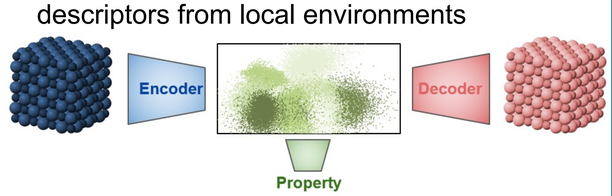

- Using a variational autoencoder (VAE) to embed a property into the global descriptor

Gharakhanyan, Shirokawa, Alsoulah, Artrith, Urban, *ICLR 2023 ML4Materials workshop* (2023).

Batteries (Energy Storage)

Example Project: Understanding the onset of surface degradation in $LiNiO_2$ cathodes

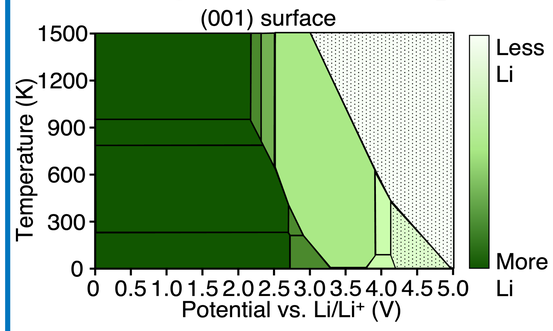

- Developed theory for surface phase diagrams of intercalation cathodes
- Revealed relationship between surface oxygen release and Ni migration

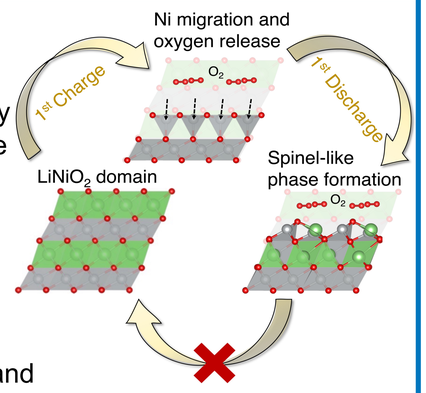

Li, Wang, Guo, Artrith, Urban, *ACS Appl. Energy Mater.* **5** (2022), 5730–5741.

Example Project: Stacking-Fault Enhanced Oxygen Redox in Li_2MnO_3

- Computed voltage profiles for Li_2MnO_3 show that stacking faults (SF) become stable during Li extraction
- SF-Li_2MnO_3 explains experimental observations correlating NMR measurements and observed capacity

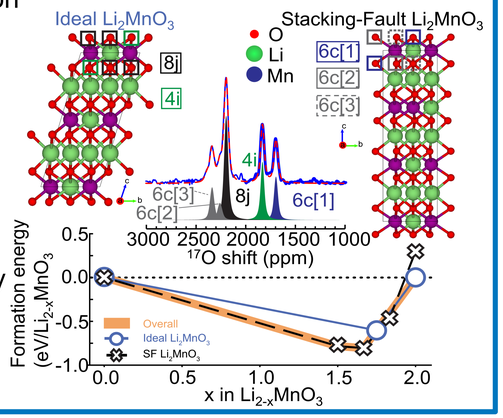

Li, Li, Monluc, Chen, Tang, Chien, Feng, Hung, Gan, Urban, Hu, *Adv. Energy Mater.* **12** (2022), 2200427.

Electrocatalysis (Energy Conversion)

Example: Membrane-coated Electrocatalyst

- Collaboration with Esposito group
- Developed theory of interface Pourbaix diagrams
- The SiO_2/Pt interface changes with the pH value and the potential
- This has potential implications for catalyst design *metal-coating synergy*?

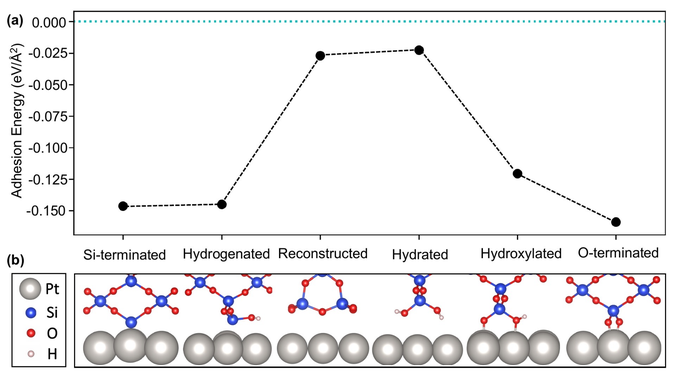

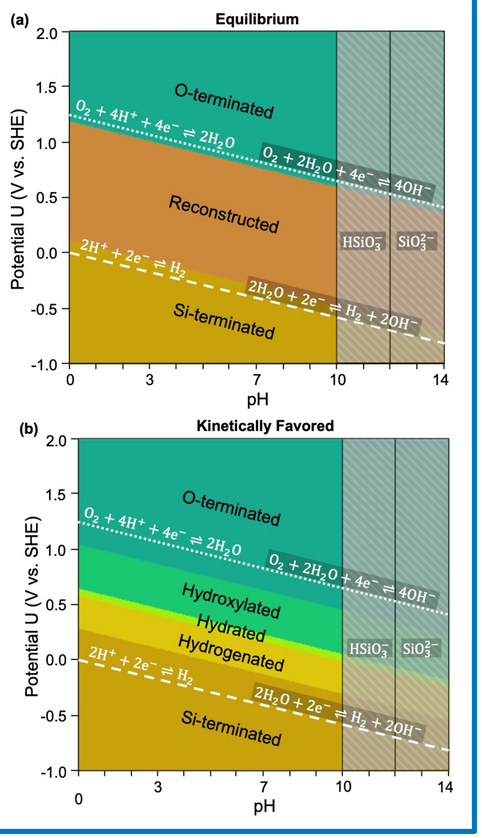

J. Qu and A. Urban,
ACS Appl. Mater. Interfaces **12** (2020) 52125–52135.